bioRxiv preprint doi: https://doi.org/10.1101/694661; this version posted November 21, 2019. The copyright holder for this preprint (which was not certified by peer review) is the author/funder. All rights reserved. No reuse allowed without permission.

Magnetic resonance measurements of cellular and sub-cellular membrane structures in live and fixed neural tissue

Nathan H. Williamson[1 *], Rea Ravin [1,2 *], Dan Benjamini[1,3], Hellmut Merkle[4], Melanie Falgairolle[4], Michael J. O'Donovan[4], Dvir Blivis[4], Dave Ide[4,5], Teddy X. Cai[1], Nima S. Ghorashi[6], Ruiliang Bai[7,1], and Peter J. Basser[1] ✉

[1] *Eunice Kennedy Shriver* National Institute of Child Health and Human Development, National Institutes of Health, Bethesda, MD, USA
[2] Celoptics, Rockville, MD, USA
[3] Center for Neuroscience and Regenerative Medicine, Henry Jackson Foundation, Bethesda, MD, USA
[4] National Institute of Neurological Disorders and Stroke, National Institutes of Health, Bethesda, MD, USA
[5] National Institute of Mental Health, National Institutes of Health, Bethesda, MD, USA
[6] Cardiovascular Branch, National Heart, Lung, and Blood Institute, National Institutes of Health, Bethesda, MD 20892
[7] Interdisciplinary Institute of Neuroscience and Technology, Qiushi Academy for Advanced Studies, Key Laboratory of Biomedical Engineering of Ministry of Education, College of Biomedical Engineering and Instrument Science, Zhejiang University, Hangzhou, China
[*] N.H.W. and R.R. contributed equally to this work.

We develop magnetic resonance (MR) methods for measuring real-time changes of tissue microstructure and membrane permeability of live and fixed neural tissue. Diffusion and exchange MR measurements are performed using the large static gradient produced by a single-sided permanent magnet. Using tissue delipidation methods, we show that water diffusion is restricted solely by lipid membranes. Most of the diffusion signal can be assigned to water in tissue which is far from membranes. The remaining 25% can be assigned to water restricted on length scales of roughly a micron or less, near or within membrane structures at the cellular, organelle, and vesicle levels. Diffusion exchange spectroscopy measures water exchanging between membrane structures and free environments at 100 s^{-1}.

tissue microstructure|diffusion exchange spectroscopy | porous media | membrane permeability| NMR-MOUSE

Correspondence: ***basserp@mail.nih.gov***

Introduction

The first diffusion tensor images of brain tissue showed diffusion anisotropy in the white matter (1). It was postulated that this anisotropy is due to myelin membranes and other cellular components impeding water mobility more in the direction perpendicular to the oriented fibers than parallel to them. By process of elimination, Beaulieu concluded that the origin of diffusion anisotropy in white matter is due to axonal cell membranes (2, 3). New methods to clear lipid membranes while leaving other tissue components intact (4, 5) have confirmed directly that diffusion becomes isotropic and diffusivity approaches the value of free water after complete delipidation (6).

A characteristic of MR is that spin magnetization retains the history of motions encoded during the experimental pulse sequence (7). Diffusion MR measures the spin echo (8) signal attenuation of nuclear spins which displace randomly in the presence of a magnetic field gradient (9–11). The displacements contain averaged information about the hindrances and restrictions which the molecules experienced during their random trajectories through the microstructure. A diffusion encoding time defines how long the motions are observed. It also defines the length scales of the displacements, albeit implicitly due to the complex scaling between displacements and time for diffusion in structured media (12). In conventional diffusion MRI, the diffusion encoding time is held constant and the gradient strength is incrementally increased in subsequent scans (13). Diffusion measurements with a static gradient system work in reverse, with the gradient strength constant and the diffusion encoding time, τ, incremented (9). Both methods lead to a measured signal attenuation, an effect which can be summarized in a single variable, b (13). The diffusion MR signal from freely diffusing water with self-diffusion coefficient D_0 attenuates as $\exp(-bD_0)$(14), while water diffusing within restricted environments attenuates more slowly (15–19). The diffusion MR signal of water in heterogeneous materials such as biological tissue would be expected to contain a multitude of components arising from water in different microenvironments, which restrict water diffusion to varying degrees (20).

Interpretation and modeling of the signal attenuation from diffusion measurements on neural tissue is an ongoing area of research (21). Nonparametric data inversion techniques can model signal attenuation as arising from distributions of diffusion coefficients (22). This inversion assumes that the full attenuation is made up of a sum of multiexponenital attenuations, each with their own D value. Distribution modeling can be a way to separate water components based on their apparent mobility (23). Pfeuffer, et al. (22), along with Refs. (23, 24), suggest that the diffusion coefficient distribution can be used to investigate the microstructural properties of neural tissue.

Nuclear spins may also exchange along the diffusion coefficient distribution by moving between microenvironments, causing diffusion coefficients of components to shift and appear closer together on the distribution. Exchange can be measured from the change in apparent diffusion coefficients with encoding time (25–29). Alternatively, MR can store the spin history from one encoding b_1 during a mixing time t_m and recall it for a second encoding b_2 (30) to measure exchange along the distribution (31). The standard diffusion

bioRxiv preprint doi: https://doi.org/10.1101/694661; this version posted November 21, 2019. The copyright holder for this preprint (which was not certified by peer review) is the author/funder. All rights reserved. No reuse allowed without permission.

measurement is one-dimensional (1-D) in that there is one encoding variable b and one measured parameter D. By encoding the spins twice (b_1, b_2), the diffusion exchange spectroscopy (DEXSY) sequence becomes 2-D (31). 2-D DEXSY measures the relationship between spins' diffusion coefficients at two separate instances (D_1, D_2) to show exchanging and non-exchanging components (32–34).

The full DEXSY sampling of the 2-D $b_1 - b_2$ space (31, 32) is too time-consuming for scanning live specimen. Recent research shows that there is some redundancy in the data (34–37) and alternative DEXSY-based approaches may measure exchange with fewer data points (34, 38, 39). Cai, et al. (39), developed a rapid measurement of the exchange fraction, f, from just four points in the $b_1 - b_2$ space. DEXSY-based methods have been shown to measure the permeability of cell membranes to water (38, 40).

Larger gradient strengths and gradient durations probe smaller structures (10). Hardware constraints cap the maximum strength of gradient coils of MRI systems at a few Tesla/m. With long gradient pulse durations and encoding times, diffusion MR microstructural resolution is predicted to be limited to structures larger than a few microns (41). However, when water within these structures exchanges on a timescale faster than the diffusion encoding time the structure sizes appear inflated, and in the extreme case of fast exchange the structures are no longer visible as attenuation measures only the mean diffusivity (26, 42). Gradient pulses last at least a millisecond, which sets a lower limit for the encoding time (43). Surprisingly, an experiment dating back to the origins of MR (8, 9), performed in a large static gradient field, can break this microstructural resolution limit (44). Low-cost, portable, bench-top, single-sided NMR devices with greater than 10 T/m static gradients (45) can probe submicron structures (46) that ordinarily cannot be resolved from larger microscale structures using state-of-the-art pulsed gradient MR systems with lower maximum gradient strengths (47). Displacement encoding within a static gradient field occurs by using radiofrequency (RF) pulses (8, 9) to switch the "effective gradient" (11), allowing for diffusion encoding times as short as 100 μs (48). This permits resolution of submicron structures that can contain rapidly exchanging water pools (46). The static gradient 1-D diffusion (49) and 2-D DEXSY (50) experiments can then be used to probe cellular and sub-cellular components and water exchange between them.

In this paper we adapt 1-D diffusion and 2-D diffusion exchange methods to perform measurements with a single-sided MR system having static gradients, to investigate the cellular and sub-cellular structures in isolated neonatal mouse spinal cord. We develop a system to support both live and fixed spinal cords during NMR measurements such that data could be compared directly. We present both unprocessed raw signal data (made available as Supplementary material) and processed diffusion coefficient distributions. Diffusion coefficient distributions show signal from water in various free and restricted environments. Diffusion signal attenuation can isolate signal from water restricted within structures smaller than a micron indicating that sub-cellular structural resolution is achieved. DEXSY reveals the water pools that exchange between restricted and free environments on a timescale of 10 milliseconds, indicating that sub-cellular membrane structure can only be measured with encoding times less than 10 ms. Replacing the protons of water with deuterium (D_2O) decreased the signal from all components of the distribution equally, indicating that the majority of the signal is coming from water. Delipidation of membranes by the surfactant Triton X indicated that restriction was caused by lipid membranes and not proteins.

Results

System provides high sensitivity to motion and restricted motion within spinal cords. The single-sided magnet's field strength decreases rapidly with distance from the top surface, with a gradient of $g = 15.3$ T/m. With diffusion measurements, g provides a nominal resolution to displacements of water on the order of the dephasing length $l_g =$ 800 nm (see Supplementary theory in SI). Signal from water which diffuses an average distance l_g significantly dephases and thus attenuates (subtracts from) the total measured signal. The diffusion encoding time τ is incremented to increase the average distance which water displaces $l_d = \sqrt{D_0 \tau}$ (with free diffusion coefficient D_0) relative to l_g. One benefit of diffusion measurements with a large static gradient is that free water signal is efficiently attenuated (the shortest τ for a given g), whereas signal from water which is restricted persists, allowing for the identification of restricted and free water at very short time and length scales. With $g = 15.3$ T/m and $D_0 = 2.15 \times 10^{-9} \mathrm{m}^2/\mathrm{s}$, freely diffusing water has significantly attenuated by $\tau > 0.3$ ms ($l_d > l_g = 800$ nm) and the remaining signal is mostly made up of water for which diffusion is impeded on that time and length scale. At $b \times D_0 = 6$ (for which $\tau = 0.63$ ms and free water moves on average $l_d = \sqrt{D_0 \tau} = 1.16\ \mu\mathrm{m}$), freely diffusing water signal has attenuated to $\exp(-6) = 0.0025$ which is approximately the standard deviation of the noise. Signal at $b \times D_0 = 6$ (or the nearest data point) is used to define the restricted water fraction. Alternatively from diffusion coefficient distribution analysis, integrals of $P(D/D_0)$ on either side of $D/D_0 = 0.17$ are heuristically used as measures of the free and restricted water fraction.

Solenoid radiofrequency (RF) coils were specially built to the size of the spinal cords under study. In the solenoid coil, the spinal cord is oriented with its length perpendicular to the gradient such that the system measures diffusion of water perpendicular to the spinal cord. Artificial cerebro-spinal fluid (aCSF) bathes the spinal cord and RF coil and provides nutrients to live tissue.

The free diffusion coefficient is defined as the diffusion coefficient of aCSF at 25°C, $D_0 = 2.15 \times 10^{-9}\ \mathrm{m}^2/\mathrm{s}$, found by monoexponential fits (see Supplementary Information (SI) Fig. S1). aCSF is well described by a single diffusion coefficient. Error residuals are random with standard deviation (SD) consistent with the noise of the system. Distributions of diffusion coefficients from data inversion are

bioRxiv preprint doi: https://doi.org/10.1101/694661; this version posted November 21, 2019. The copyright holder for this preprint (which was not certified by peer review) is the author/funder. All rights reserved. No reuse allowed without permission.

non-dimensionalized by D_0 such that the aCSF distribution should be a delta function at $D/D_0 = 1$. The inversion method smooths and broadens the aCSF distribution (Fig. 1 c) due to regularization which is needed to stabilize distribution estimates (51).

Signal was acquired from a 400 μm slice through the spinal cord sample and aCSF bathing the sample. The contribution from the aCSF surrounding the sample needed to be quantified. Fig. 1 shows distributions of diffusion coefficients for a fixed spinal cord placed within the RF coil and bathed in aCSF (a) and after removing the aCSF from the RF coil using a pipette and kimwipes, leaving only the sample and the fluid within the sample (b). These can be compared to the distribution from only aCSF filling the RF coil (c). Differences in the free diffusion component fraction indicates that aCSF accounts for only 5% of the signal in (a). The solenoid coil itself does an excellent job isolating signal from the spinal cord sample filling its interior.

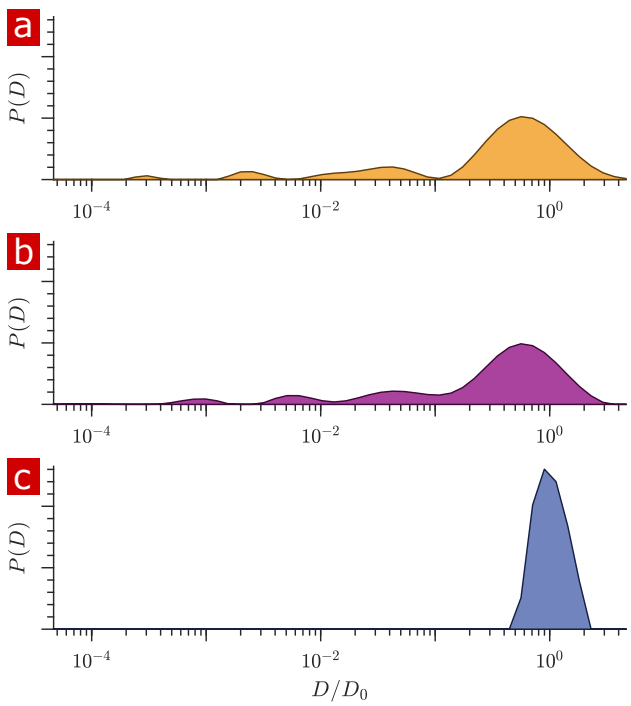

Fig. 1. Diffusion coefficient distributions. a) Distribution of diffusion coefficients from a fixed spinal cord bathed in aCSF. b) Distribution from the same spinal cord after removing the aCSF bath. c) Distribution from only aCSF filling the RF coil.

1-D diffusion measures 25% of water to be restricted. Signal attenuation and diffusion coefficient distributions from 1-D diffusion measurements performed on a fixed spinal cord specimen are presented in Fig. 2. Signal attenuation from measurements of pure aCSF is also shown for comparison. Signal is plotted as a function of the non-dimensionalized diffusion encoding variable $b \times D_0$. Exponential attenuation is expected for fluids diffusing freely, as shown by Eq. S1. N.B. The largest b ($\tau = 6.6$ ms) corresponds to 3,000,000 $\mathrm{s/mm^2}$, two to three orders of magnitude larger than what is typically reached in conventional pulsed gradient diffusion MRI studies. aCSF signal is mono-exponential and quickly attenuates to the background noise level. This background noise is Gaussian with $\mathrm{mean} = 0.001$ and $\mathrm{SD} = 0.002$ (see SI Fig. S2 c). Spinal cord signal attenuation is multiexponential over the entire range of b and does not fully attenuate, implying the presence of multiple highly restricted pools. System characteristics led to high SNR (> 500) diffusion measurements such that signal could be observed at extremely high diffusion weightings (see Methods). The signal intensity from 30 measurements performed on the same sample over the course of 30 hours varied similarly to the background noise (see SI Fig. S2 a and b). Measurement variability is thus simply determined by the signal-to-noise ratio (SNR) and the system is amenable to long scans and signal averaging.

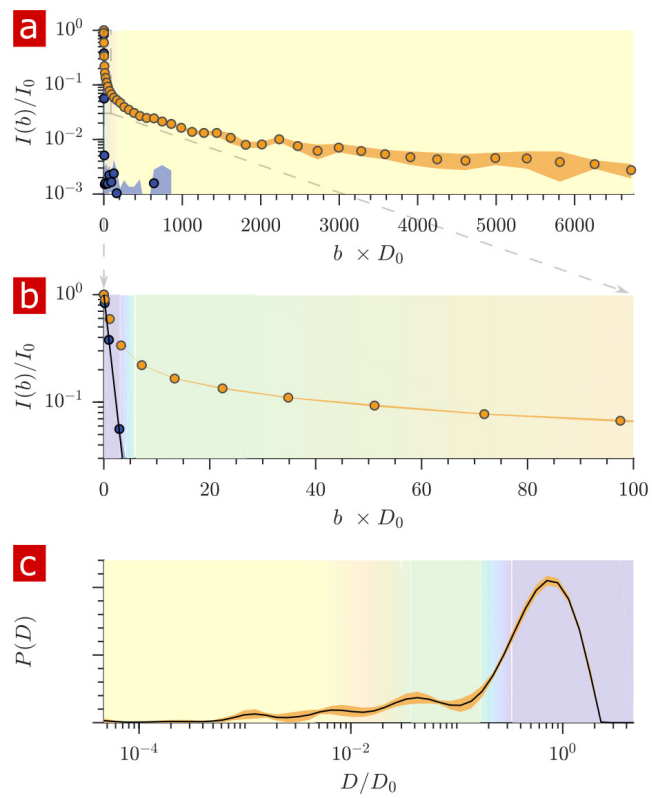

Fig. 2. Diffusion measurement of a fixed spinal cord. a) Mean (circles) and SD (shaded bands) of the signal intensity from five diffusion measurements, spaced 54 minutes apart, performed on a fixed spinal cord (orange) and three measurements performed on aCSF (purple) at 25°C. b) Signal intensity from the zoomed in area shown in (a). c) The distribution of diffusion coefficients resulting from inversion of the data. The purple, green, and yellow shading across plots signifies water which is free, less restricted, and more restricted, respectively. Models of signal attenuation (Eqs. S1–S5) are used to define the cutoffs for each of these regimes based on when their signal components would attenuate to $\exp(-6)$. Values are inverted to define the color shading on the D distribution. This inversion of colors is simply to guide the eye. The color gradient is meant to signify a continuous change between diffusion regimes rather than sharp boundaries.

The distribution of apparent diffusion coefficients is shown in Fig. 2 (c). The majority of the distribution is made up of free water. Humps extending to lower values of D/D_0 represent signal which is more and more restricted and on smaller length scales, as indicated by the color gradient.

Both the signal attenuation and the distributions show that

bioRxiv preprint doi: https://doi.org/10.1101/694661; this version posted November 21, 2019. The copyright holder for this preprint (which was not certified by peer review) is the author/funder. All rights reserved. No reuse allowed without permission.

the mobility of a large portion of water is restricted to some degree during the diffusion encoding time. The restricted fraction quantified from distribution analysis is (mean $\pm$ SD) 0.23 ± 0.006. Alternatively from raw signal, the restricted fraction is 0.22 ± 0.002. Taking into account a few percent of the free water component being from aCSF bathing the sample, roughly 25% of the water in the tissue is restricted on the 1 ms timescale.

Full DEXSY measures water exchanging between free and restricted environments 100 times per second. 2-D DEXSY labels spins based on their local mobility at two instances which are separated by the mixing time variable t_m (31). This permits the direct measurement of water movement from one environment (e.g. A) to another (B) as well as water moving in reverse (B) to (A) to fulfill mass conservation. In the case that water exchanges between environments on intermediate timescales (greater than the diffusion encoding time and less than the longitudinal relaxation time T_1 which causes spins to forget their encoding), the exchange increases and saturates as a function of t_m (34, 39, 52, 53). The classic analysis of DEXSY is as a joint 2-D probability distribution showing relationships between the apparent diffusion coefficients of water populations during the first encoding period, D_1 and the second encoding period D_2 (32, 34). Integrated probability density at a point or region (D_1, D_2) indicates the probability of a spin being at D_1 during encoding 1 and D_2 during encoding 2. Non-exchanging water populations have $D_1 = D_2$, defining a diagonal line across the distribution, whereas exchanging water populations are located off the diagonal. A representative 2-D DEXSY distribution for a spinal cord is shown in Fig. 3 (a). The distribution is divided into a 3x3 grid for the possible exchange pathways between components A ($2.6 \times 10^{-4} - 4.7 \times 10^{-2}$), B ($4.7 \times 10^{-2} - 1.5 \times 10^{-1}$), and C ($2.6 \times 10^{-1} - 4.7 \times 10^{1}$ D/D_0), shown by the color coding and labels. This division was chosen in an attempt to separate the free water component (C) from the restricted water component, and to separate the restricted component into two groups (B and A) based on their apparent mobility. The integrated probability density from each region represents an exchange (off-diagonal) or non-exchange (on-diagonal) fraction. The distribution shows exchange between free water and restricted water. Additionally, there appears to be exchange between restricted components. Stacked plots at $t_m = 0.2$, 4, 20, and 160 ms (b) show the increase in probability for components exchanging with free water, regions $\mathrm{AC} + \mathrm{CA}$ and regions $\mathrm{BC} + \mathrm{CB}$ and a decrease in probability for the non-exchanging components, e.g., region AA appears to decrease to near zero at the longest t_m.

The build-up of exchange fractions and decay of non-exchange fractions over t_m are fit with a first order rate equation to obtain apparent exchange rates (AXRs) (SI Fig. S3). Measurements on five different spinal cords show consistent exchange behavior. Restricted components exchange with free water with AXR$\approx$100 s^{-1}. $f_{\mathrm{AB+BA}}$ does not increase with t_m, indicating that the DEXSY measurement is primarily sensitive to water exchanging between restricted and free environments and not between and among different restricted environments.

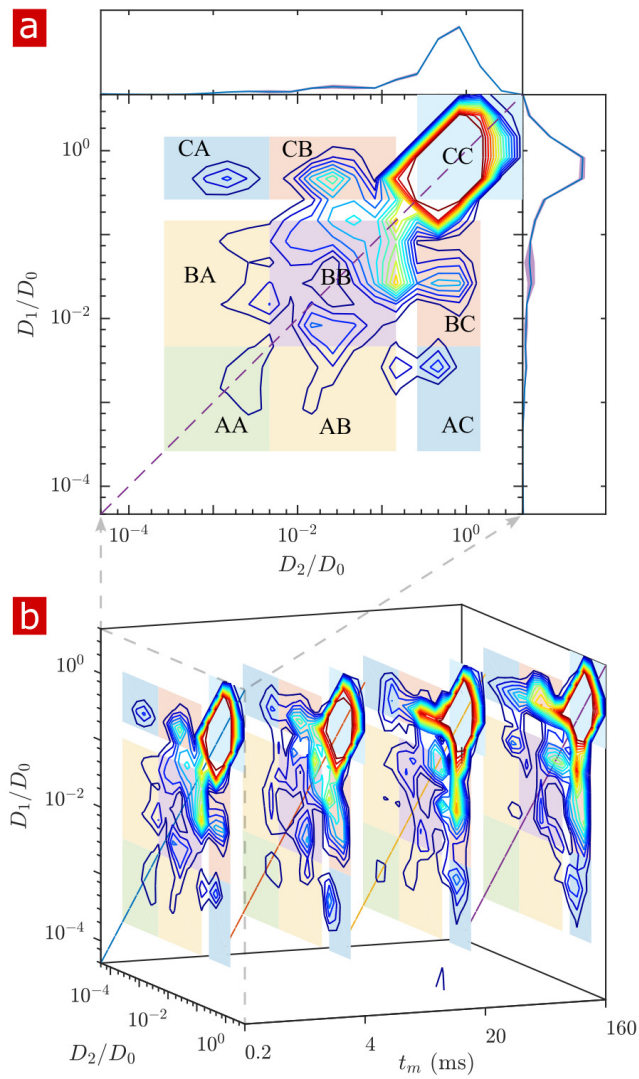

Fig. 3. Full 2-D DEXSY diffusion exchange distribution for a fixed spinal cord. a) Exchange distribution measured with mixing time $t_m = 0.2$ ms. Distributions show exchanging (off-diagonal) and non-exchanging (on-diagonal) components. These components are lumped into regions A, B, and C, shaded and labeled in a 3×3 grid for each exchange combination. The range of $P(D_1, D_2)$ is set to add detail to components A and B, but cuts off the top of the most mobile region CC. The marginal distributions $P(D_1)$ and $P(D_2)$ are presented on the sides, with mean (solid blue lines) and SD (shaded bands around lines) from 3 measurements. b) A stacked view of distributions measured with mixing time $t_m = [0.2, 4, 20, 160]$ ms. With increasing t_m, the probability density builds up in regions of free and restricted water exchange $\mathrm{AC} + \mathrm{CA}$ and $\mathrm{BC} + \mathrm{CB}$ and decays for non-exchanging restricted water regions AA and BB. The build-up and decay is quantified in Fig. S3.

Rapid exchange measurement agrees with full DEXSY. Full DEXSY measurements at four mixing times took eight hours—too long to measure exchange in living tissue. Therefore, we strove to develop a method to rapidly measure exchange (39) (see SI). The rapid measurement provides an apparent exchange fraction f, a diffusion-weighted average of exchange between all water pools. The full DEXSY can resolve multiple exchanging water pools and the exchange pathways between them (54, 55). Although the rapid measurement lacks the full DEXSY's resolution of multi-

bioRxiv preprint doi: https://doi.org/10.1101/694661; this version posted November 21, 2019. The copyright holder for this preprint (which was not certified by peer review) is the author/funder. All rights reserved. No reuse allowed without permission.

component exchange, it provides enhanced temporal resolution, both with respect to t_m and experimental time, by sidestepping the need for 2-D data inversion (56) and by acquiring the data much more rapidly. The protocol used here acquired the data at one exchange fraction (one mixing time) per minute.

Exchange fractions from the rapid measurement are presented in Fig. 4 for the same specimen as used for the full DEXSYs (Figs. 3 and S3). The AXR from three repeat measurements was $110 \pm 30\ \mathrm{s}^{-1}$. This value is not different statistically from the results of the full DEXSY measurement, validating the rapid measurement method. Additionally, the value from repeated measurements on five fixed samples was $110 \pm 20\ \mathrm{s}^{-1}$ at 25°C (mean ± SD taken across all 3×5 measurements), indicating high reproducibility between specimen. (Sample-to-sample variability of AXRs is presented in Fig. S4.)

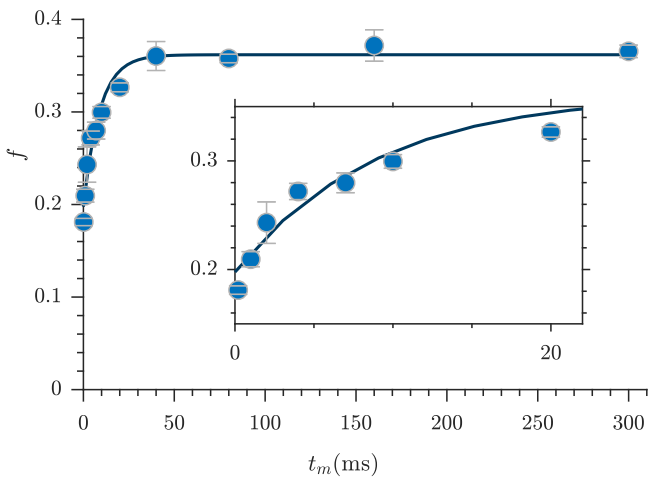

Fig. 4. Rapid measurement of exchange fractions. A fit of the first order rate model estimated an apparent exchange rate, AXR = $110 \pm 30\ \mathrm{s}^{-1}$ (mean ± SD from three measurements performed at 25°C). Inset shows a zoomed-in region of the initial rise in exchange.

Restricted diffusion measures sub-micron structures.

After free water has fully attenuated, restricted water signal attenuation is exponential with the diffusion encoding time τ and the size of the restriction (15–19), as presented in Eqs. S2–S5. Attenuation models for water restricted in spheres of radius R indicate that with $g = 15.3$ T/m the diffusion experiment provides a 200–1400 nm window on restriction radii (Fig. 5 (a)). Signals from water in restrictions smaller than $R = 200$ nm do not attenuate significantly enough to differentiate. In restrictions larger than R=1400 nm, signal from water far from surfaces attenuates as free water and signal from water near surfaces attenuates as localized water (restricted on one side but free on the other). The long-time behavior of the diffusion signals are analyzed to estimate a radius of restriction in Fig. 5 (b). Exchange also causes attenuation which is exponential with τ (46). The estimate accounts for attenuation due to exchange, utilizing the measured AXR. The estimated radius is $R = 900$ nm. This can be viewed as a volume-averaged restriction length, filtering out water in structures with $R > 1400$ nm.

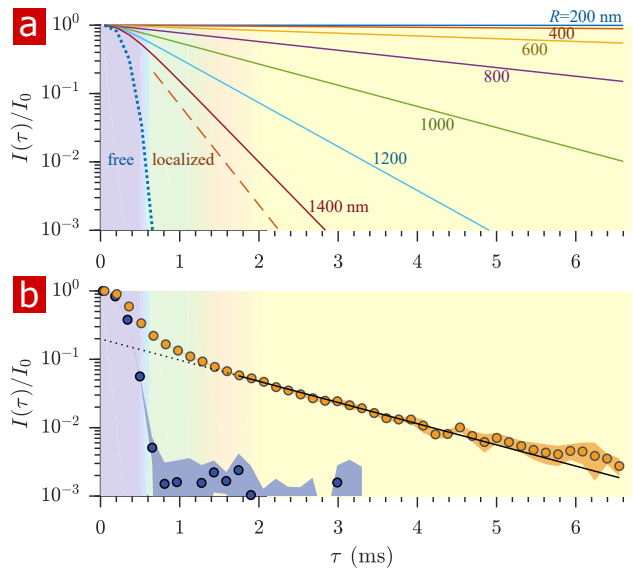

Fig. 5. Estimating membrane structure sizes from the diffusion signal attenuation. a) Signal intensity is simulated for water restricted in spherical compartments of varying radius between $R = 200 - 1400$ nm (Eq. S3, solid lines) (17), for water localized near a surface in larger restrictions (Eq. S2, red dashed line) (18, 19), as well as water diffusing freely (Eq. S1, purple dotted line) (14). Signal is plotted as a function of the variable τ (rather than $b \sim \tau^3$). b) Signal is re-plotted from Fig. 2. Signal at $\tau \geq 1.8$ ms is fit with the model for water restricted in spherical compartments in the limit of long τ (Eq. S5, solid black line) (17) incorporating the AXR=110 s^{-1} (46), estimating a radius $R = 900$ nm. The dotted black line extrapolates back to $I/I_0 = 0.2$. Color shading is similar to Fig. 2.

NMR recordings do not affect viability of spinal cord.

The signal attenuation from diffusion measurements performed on live spinal cords (n = 9) is compared to that of fixed spinal cords (n = 6) and only aCSF in Fig. 6 (a). The signal attenuates slightly faster although not significantly as seen by the standard deviations. The mobility of water on the timescale of milliseconds is very similar in live and fixed specimen. (Sample-to-sample variability of signal attenuation is presented in Fig. S5.)

After two hours of NMR measurements and four to seven hours post-dissection, spinal cords (dissected on postnatal (P) day P2, P3, and P4) were assessed for viability by recording motoneuronal electrical activity after stimulation of a dorsal root. Mono- and polysynaptic reflexes were recorded in all preparations (n = 4), Fig. 6 (b), indicating that neither the experimental setup nor the protocol compromised the neuronal excitability of the spinal cord.

NMR measurements are primarily sensitive to water.

To determine whether biomacromolecules were contributing to the signal observed in the spinal cords, rapid exchange and 1-D diffusion measurements were recorded in real-time as a fixed spinal cord was washed with aCSF made with 99.8% deuterium water (D_2O aCSF). (Results are presented in Fig. S6). After two successive washes, proton signal decreased to values similar to D_2O aCSF alone. All diffusion coefficient distribution components decreased similarly after D_2O washing. Components of the distribution which are not from water would still remain after removing H_2O. Therefore, all distribution components are primarily made up of water. This

bioRxiv preprint doi: https://doi.org/10.1101/694661; this version posted November 21, 2019. The copyright holder for this preprint (which was not certified by peer review) is the author/funder. All rights reserved. No reuse allowed without permission.

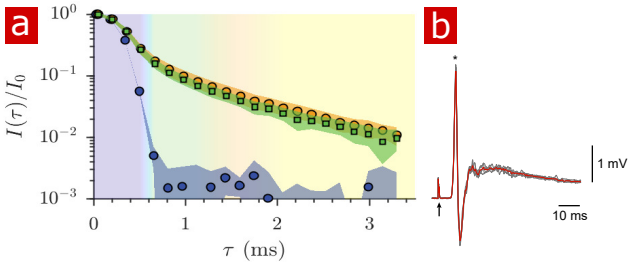

Fig. 6. Diffusion in fixed vs. live. a) Signal intensity from diffusion measurements performed at 25°C on live samples (n = 9) (green squares), fixed samples (n = 6) (orange circles) and aCSF (purple circles) plotted as a function of the variable τ. (b) Mono- and poly- synaptic reflexes were recorded from the L6 ventral root of live samples (n = 4) after NMR measurements. Stimulation was done on the homonymous dorsal root. The grey lines are 5 successive stimuli (30 s interval) and the superimposed red line is the average signal. The arrow indicates the stimulus artifact and the star the monosynaptic reflex.

points to water rather than biomacromolecules accounting for the vast majority of the measured signal.

Delipidation shows membranes to be the sole source of restriction. Triton X surfactant was used to remove lipid membranes from spinal cords in order to determine the effect of membranes on water restriction. The aCSF bathing the spinal cord was replaced with aCSF with Triton X while rapid exchange and 1-D diffusion measurements were repeatedly performed (n = 2). Fig. 7 shows exchange fractions (a) and 1-D distributions from select time points (b).

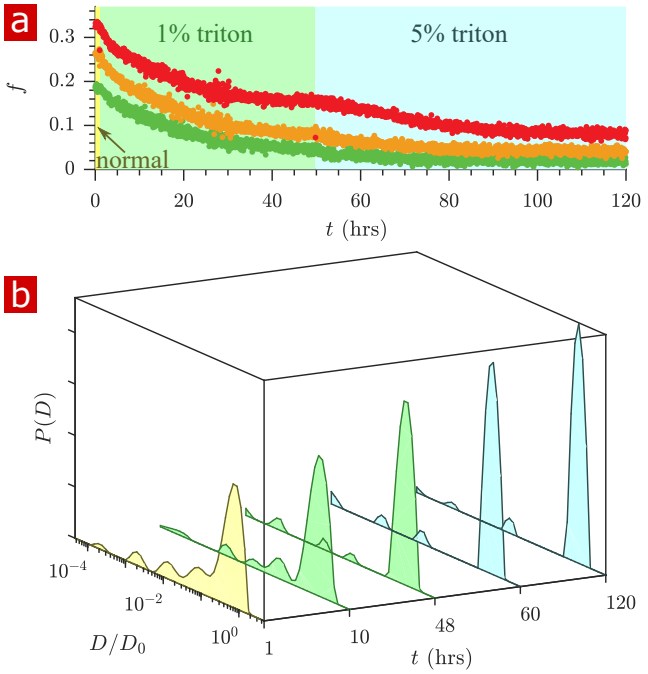

Fig. 7. Timecourse study of Triton X delipidation. a) Exchange fractions from rapid exchange measurements with $t_m = 0.2$ (green dots), 4 (orange dots), and 20 ms (red dots) measured throughout the timecourse, as the sample was washed to aCSF with 1% Triton X, and then 5% Triton X. b) Representative diffusion coefficient distributions from 1-D diffusion measurements performed at different times before and after addition of Triton.

After the addition of 1% Triton X at 1 hr, the exchange fractions decreased slowly and reached a plateau. Washing to 5% Triton X at 50 hrs decreased the exchange fractions further until they again reached a plateau.

The diffusion coefficient distributions (Fig. 7(b) and Supplementary movie S1) show that the delipidation process removed the barriers for restriction. Therefore, lipid membranes, not the remaining biomacromolecules, are the source of restriction of water diffusion. The fraction of restricted water (Fig. S7 c) decreases and plateaus similarly to the exchange fractions.

About 6% of the signal appears restricted after 120 hrs of delipidation. This is signal from Triton X, which as a 5% solution imparts a 6% signal at $D/D_0 = 0.01$ (see Fig. S8). Samples (n = 2) were also studied after full delipidation and washing away Triton X (Fig. 8). The diffusion signal attenuation, (a) and (b), shows that 95% of the signal is monoexponential with $D/D_0 = 0.90$. The diffusion coefficient distribution (c) shows one major free diffusion peak which is not significantly different from the diffusion coefficient distribution of pure aCSF. Some small peaks which are not seen unless $P(D)$ is magnified lead to a 1% restricted component (also seen in the raw signal). This 1% component may be residual Triton X which remained after washing. Without membranes there is essentially only one diffusive environment throughout the whole sample.

Discussion

We present NMR methods which use the diffusion of water to probe cellular and sub-cellular membrane structures on sub-millisecond and millisecond timescales. Much of the advance was possible because the large static gradient overcomes (44) many hardware (43) (e.g. slew rate, eddy currents, maximum gradient strength) and biological (e.g. peripheral nerve stimulation (57)) limitations of pulsed gradients. In 1996 Köpf, et al., realized this capability on biological tissue, performing diffusion measurements using a 50 T/m static gradient in the stray field of a superconducting 9.4 T magnet (58). Another stray field study by Carlton, et al., used an 18 T/m static gradient to measure bacteria concentrations (46). Bacteria are roughly a micron in diameter, similar to sub-cellular structures in tissue. They noted the static gradient experiment provided more intracellular signal compared to pulsed gradient experiments on bacterial systems (47) due to less exchange during the shorter diffusion encoding time. We re-purposed a low field single-sided permanent magnet (45) which, due to its profiling capabilities (59), has found a number of niche applications in materials science and engineering, biology and medicine, and cultural heritage (60–62). The large 15.3 T/m gradient allowed for the attenuation of tissue water signal below $I/I_0 = 0.01$ in a diffusion encoding time of 6.6 ms.

A large SNR and Gaussian zero mean noise was necessary to resolve slowly attenuating signals above the noise and to not confuse the signal with a baseline noise floor. In general, SNR > 100 is needed for diffusion coefficient distribution analysis (63) and as a rule-of-thumb this allows for resolution of populations comprising as little as 1% of the signal. Performance tuning led to very stable measurements and SNR > 500. These modifications included a 2000 echo CPMG readout, 25 μs echo time, a sample-specific solenoid

bioRxiv preprint doi: https://doi.org/10.1101/694661; this version posted November 21, 2019. The copyright holder for this preprint (which was not certified by peer review) is the author/funder. All rights reserved. No reuse allowed without permission.

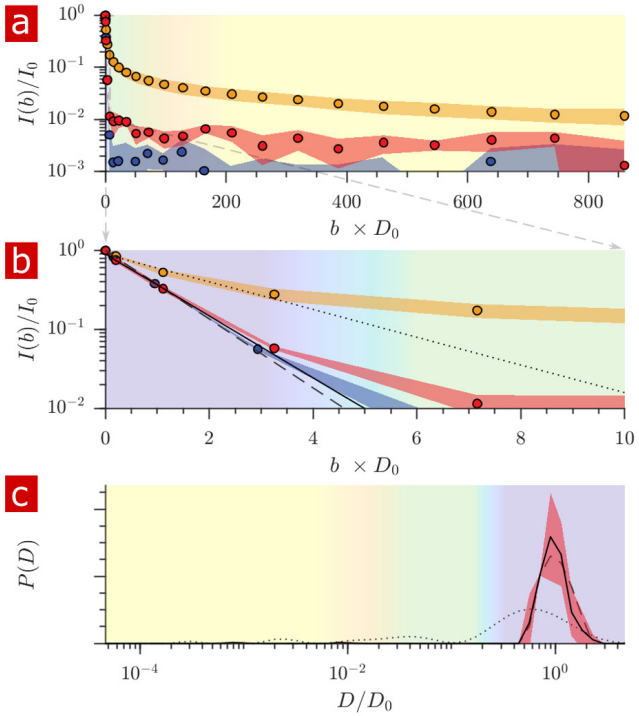

Fig. 8. Diffusion measurement after delipidation. a) Diffusion signal intensity from measurements on spinal cords performed at 25°C after delipidation (n = 2) with 10% Triton X and after washing the Triton away. The mean (circles) and SD (shaded bands) of the attenuation are plotted for the delipidated samples (red) alongside pure aCSF (purple) and fixed undelipidated spinal cords (n = 6) (orange). b) The initial attenuation of signal. Monoexponential fits of the attenuation from points 2–4 yielded 2.15 ± 0.01, 1.94 ± 0.02 and $0.87 \pm 0.14 \times 10^{-9}$ m^2/s for the aCSF, delipidated, and undelipidated spinal cords and are shown as the dashed, solid, and dotted lines respectively. c) Diffusion coefficient distribution of the delipidated spinal cords, for which the mean (solid line) and SD (shaded band around line) are not significantly different from the pure aCSF (dashed line). The distribution from a fixed, undelipidated spinal cord (dotted line) is also shown for comparison. The purple, green, and yellow shading across the plots signifies water which is free, localized, and restricted.

RF coil, a wet/dry chamber without circulation, and noise reduction/isolation.

High SNR and system stability led to highly reproducible data (Fig. S2). Based on the standard deviation of the normalized signal from repeat measurements, $\mathrm{SD}/I_0 = 1/\mathrm{SNR} = 0.002$, pathological or physiological events which cause slight variation of the diffusion-weighted signal may be detectable (e.g. $2 \times \mathrm{SD}/I_0 = 0.004$ for 95% confidence assuming Gaussian errors). This level of sensitivity is similar to what is reported for state-of-the-art preclinical animal diffusion MRI, e.g. diffusion functional MRI of the rat brain ($\mathrm{SD}/I_0 = 0.003$, one scan, $1.5 \times 0.23 \times 0.23$ mm voxels) (64). The study of live *ex vivo* tissue removes the variability associated with *in vivo* studies such as blood flow and motion. The open design of the NMR experimental setup facilitates real-time measurements during perturbations to the sample.

The variability of diffusion signal was much larger across samples (Fig. S5) than across measurements repeated on the same sample (Fig. S2). The additional variability may be due to structural and size differences between samples. In contrast, rapidly measured AXRs showed similar variability across samples and across repeat measurements (Fig. S4). This would indicate that AXR variability was primarily driven by SNR and not differences between samples. The AXR is not sensitive to differences in the fraction of the measurement volume taken up by bulk fluid. Bulk fluid far from the tissue does not exchange on the timescale of the measurement and does not impact the AXR. Therefore, unlike the diffusion signal, the AXR is insensitive to sample size differences and large-scale structural differences. In the exchange measurement, the heterogeneity in mobility which is encoded in < 1 ms fully exchanges and reaches a steady-state by 300 ms (Fig. 4. The AXR is sensitive to average surface-to-volume and permeability characteristics which are quite local (within 10s of microns) to the membranes. These characteristics appear similar between samples.

The solenoid RF coil permitted low-power, 2 μs RF pulses, high filling factor, and maximized signal from the spinal cord filling its interior relative to aCSF. Previous studies on live *ex vivo* neural tissue utilized MR imaging (29, 65–69). However, their analysis was on regions of interest (ROIs) which encompassed the entire sample, indicating that no additional specificity was obtained from the imaging. Because 95% of the signal came from spinal cord tissue, imaging was not necessary. This let us achieve high SNR and sufficiently rapid measurements.

The wet/dry chamber kept the liquid environment still while the gas environment provided oxygenation. Previous diffusion MRI studies on live *ex vivo* neural tissue provided oxygen to the sample through perfused aCSF (29, 65–70). Media perfusion can cause convection artifacts in the diffusion measurement (71). Researchers typically implemented start-stop diffusion MR protocols, with aCSF perfusion between MR measurements (67, 68). However, a steady concentration of oxygen is preferable and better represents the *in vivo* environment. The wet/dry chamber provided a constant supply of oxygen to the tissue while avoiding convection artifacts, creating ideal conditions for diffusion measurements on live tissue.

Neonatal mice were studied rather than adult mice because viability of *ex vivo* spinal cords is known to decrease with age (72). *Ex vivo* Spinal cords become more prone to hypoxia as they grow larger and oxygen in the tissue is consumed faster than it can diffuse to the center (73). We directly demonstrate that spinal cords are alive after hours of NMR measurements by recording electrical responses from motoneurons.

Our novel experimental setup reveals signal from highly restricted pools. We determined that these pools are exclusively membrane-restricted water. Previous nerve tissue studies reported resolvable water mobility components spanning two orders of magnitude on the diffusion coefficient distribution (20, 22–24)). Here, distributions showed components with diffusivities three orders of magnitude lower than free water. Similar values have been reported for other, larger, proton bearing molecules naturally occurring in biological tissue (74). However, by replacing the water in the tissue with deuterated water, we determined our methods to be sensitive

bioRxiv preprint doi: https://doi.org/10.1101/694661; this version posted November 21, 2019. The copyright holder for this preprint (which was not certified by peer review) is the author/funder. All rights reserved. No reuse allowed without permission.

primarily to protons on water and not protons on biomacromolecules.

Diffusion measurements with a large static gradient separate free water from restricted water because freely diffusing water attenuates exponentially with b whereas water which feels the boundaries of membranes attenuates exponentially with $b^{1/3}$ (75) (which is proportional to τ, as used for the abscissa in Fig. 5) after the free water component has attenuated. The linearity of the attenuation at long τ (in Fig. 5) provides an additional signature of restricted water.

Data inversion methods used to obtain 1- and 2-D distributions of diffusion coefficients assume that the data attenuates exponentially with b. This is only valid for a particular range of the signal attenuation, and a component that, e.g., attenuates exponentially with $b^{1/3}$ will appear to attenuate multiexponentialy with b and thus result in a distributed component when inverted. Regularization is used to stabilize distributions in the presence of noise and has the effect of smoothing the distribution. The smoothing suppresses the artifactual "pearling" of distributions into multiple peaks but broadens the peaks which should be sharp such as observed for aCSF (Fig. 1) (76). A conservative approach was taken in the regularization (discussed in the methods) and when interpreting the distributions as showing free and restricted components. In particular, individual peaks in the restricted region are not interpreted as arising from individual compartment types or sizes. New development of nonparametric diffusion models may allow further interpretations.

The free water peak of the diffusion coefficient distribution accounts for 99% of the water (Fig. 8), vs. roughly 75% of the water before delipidation. Signal attenuation is monoexponential with $\langle D \rangle / D_0 = 0.90$, vs. multiexponential with $\langle D \rangle / D_0 = 0.40$ before delipidation. Deviation from monoexponential, Gaussian signal attenuation is due to restriction by lipid membranes. From micron (2, 3, 6) to sub-micron length scales, water restriction in tissue is due solely to membranes.

After removing restrictions, hindrances to water diffusion can be thought of as arising from volume obstruction by biomacromolecules such as proteins within the tissue. Obstruction models of water (solvent) self-diffusion incorporate only the volume fraction of biomacromolecules, θ, as a free parameter and are generally adequate models in the limit of low (< 0.1) volume fraction (77). Such models predict $0.03 < \theta < 0.07$ for $\langle D \rangle / D_0 = 0.90$. Neural tissue consists of 8% proteins (6) and thus can account for the obstruction effects. Leuze, et al. used another lipid clearing method to determine that lipids are the dominant source of MRI contrast. We can now additionally say that proteins act as simple obstructions, reducing water diffusion only slightly from D_0. This finding can be compared to previous reports of water diffusion in cytoplasm isolated from red blood cells, showing $\langle D \rangle / D_0 = 0.70$ (78). Although we used shorter diffusion encoding times, delipidated samples showed monoexponenital, Gaussian diffusion signal attenuation with b, indicating that microstructural information is averaged out during the encoding time and should show no additional encoding time dependence (12). The decreased diffusivity from cytoplasm (78) could arise from the presence of organelles and membrane particles still present in the supernatant after lysing and centrifuging the red blood cells.

The methods were used to follow penetration of deuterated water into the tissue as well as the delipidation of the tissue via Triton X. The timescale of water penetration was ≈ 1 min, consistent with mass transport theory, but the timescale of Triton X penetration and delipidation was ≈ 1 day, longer than predicted (≈ 3 hrs) (see Supplementary Results in SI). An increased time is expected due to the reaction front which develops as Triton X delipidates, slowing its overall penetration. No significant increase in exchange rate was observed during the delipidation timecourse. This is in contrast to reports of cationic and nonionic surfactant mixtures permeablizing the membranes of yeast suspensions to water (40). In the real-time delipidation of the spinal cord (Fig. 7), a slowly progressing front of Triton X penetrating into the tissue removes all of the membrane structures as it passes. In the rapid exchange measurement, which is averaged over the diameter of the specimen, the most robust effect is the delipidation of compartments resulting in a reduction in exchange fractions.

Theoretical models indicate that the static gradient diffusion measurement provided a window on membrane structures smaller than roughly 1400 nm. The neonatal mouse spinal cord contains mostly gray matter (79, 80). Structures smaller than 1400 nm include cells and portions of cells with small radii such as axons, dendrites, glial processes, myelin, and a number of membranous organelles such as nuclei, mitochondria, endoplasmic reticula, and vesicles (81), in addition to extracellular sheets and tunnels (82).

The estimate of restriction length R uses a theoretical model for the motional averaging regime (Eq. S5) and assumes that $R < l_g$ such that spins can diffuse across the restriction many times without significant dephasing. The localization regime, on the other hand, assumes $l_g < R$, such that water near surfaces moves and dephases slowly but can move to regions further away where it is free and dephases rapidly. $R \approx l_g$ would imply that the data falls into an intermediate regime between localization and motional averaging. Therefore, both regimes, and perhaps higher order terms to the models of attenuation in these regimes (83, 84), may be playing a part in the attenuation. Therefore, the method used to estimate R is simplified. Nonetheless, the interplay between the attenuation regimes, heterogeneity of restriction sizes, and exchange make the modeling of diffusive motion of water in biological tissue a very challenging problem, and an important topic for future research which before now could not be experimentally studied or validated.

The fixed direction of the gradient relative to the sample inhibits the study of anisotropy. Therefore, the restrictions imposed by long and slender cells and cell processes cannot be separated from restrictions of round or folded organelles. Further study is necessary to isolate the organelle contribution. Combined pulsed gradient and static gradient methods may serve beneficial for this purpose. Pulsed gradient meth-

bioRxiv preprint doi: https://doi.org/10.1101/694661; this version posted November 21, 2019. The copyright holder for this preprint (which was not certified by peer review) is the author/funder. All rights reserved. No reuse allowed without permission.

ods can measure anisotropy through variation of the gradient directions (85, 86). A combined study would be additionally beneficial by broadening the window of resolvable structure sizes (41, 87, 88).

Full 2-D DEXSY distributions showed restricted water exchanges with free water, but could not resolve exchange between restricted water pools. The rapid measurement was designed to hone in on the exchange between restricted and free water pools and AXRs were consistent with results from the full DEXSYs. Results indicate that we have developed a non-invasive, sufficiently rapid method of measuring exchange across membranes in live tissue. The AXR $\approx 100\ \mathrm{s}^{-1}$ is significantly faster than intracellular–extracellular water exchange rates measured in neural tissue ($\approx 0.5 - 5\ \mathrm{s}^{-1}$) (42, 89–92). Such fast turnovers are not unheard of, e.g. red blood cells show similar ($\approx 100\ \mathrm{s}^{-1}$) rates (25, 27, 29) due to their high expression of aquaporin (93). Veraart, et al., recently found that incorporating fast $30 - 100\ \mathrm{s}^{-1}$ exchange rates into compartmental models provided the best fit of human gray matter diffusion MRI data (94). They concluded that dendrites and unmyelinated axons which account for the majority of the neurites in gray matter have a greater permeability than myelinated axons which predominate white matter. In addition to membrane permeability, the other factor affecting exchange is the ratio of membrane surface to volume. This ratio increases with smaller structure sizes. Therefore, fast AXRs can be explained by the resolution of the system to membrane structures with high permeability and with large surface to volume ratios.

Signal attenuation from water which remains restricted during the timescale of diffusion encoding can provide sensitivity to structure sizes (95). Studies indicate that pulsed gradient diffusion methods can measure the diameter of myelinated axons which are larger than a few microns (96). Exchange is on a long enough timescale to be neglected (12, 90) such that resolution can be treated as solely limited by gradient strength (41). The fast exchange rates measured in the current work indicate that extending structure size estimation methods to neural applications beyond myelinated axons requires that both gradient and diffusion encoding time be taken into consideration. Significant exchange causes the size of structures to be overestimated. Since exchange rates increase with surface to volume ratio, the overestimation increases with decreasing structure size.

Methods

Ethics statement for animal experimentation. All experiments were carried out in compliance with the National Institute of Neurological Disorders and Stroke Animal Care and Use Committee (Animal Protocol Number 1267-18).

Test chamber and experimental conditions. The experimental test chamber (Fig. 9 (a)) was designed to support live spinal cord for hours without requiring oxygenated artificial cerebro-spinal fluid (aCSF) flow, thus avoiding flow-related measurement artifacts (71). The gas-tight wet/dry chamber was fabricated at the NIH/NIMH mechanical workshop. The assembled chamber had two environments—a static liquid environment with aCSF and above it a gas environment with a slow flow of humidified 95% O_2 and 5% CO_2 gas. The sample temperature can be controlled in the range of $7 - 37°\mathrm{C}$. Sample temperature was monitored by a PicoM fiber optic sensor (Opsens Solutions Inc., Québec, Canada) and regulated by a shallow water bath surrounding the chamber. The bottom portion of the chamber was made of aluminum to provide good heat conduction to the media. (See SI for additional information.)

In order to compare data between live and fixed tissue, oxygenated aCSF was used as the buffer solution for all experiments. A spinal cord was placed inside the solenoid RF coil within the chamber half-filled with aCSF previously bubbled with 95% O_2 and 5% CO_2. The chamber was sealed and connected to gas flow with humid 95% O_2 and 5% CO_2.

Mouse spinal cord dissection, fixation, and delipidation. All experiments were performed on Swiss Webster wild type (Taconic Biosciences, Rensselaer, NY, USA) between one day after birth to postnatal day 4. The mouse spinal cords were isolated and placed in a dissecting chamber perfused with cold Low-Calcium High Magnesium aCSF (concentrations in mM: 128.35 NaCl, 4 KCl, 0.5 $CaCl_2 \cdot H_2O$, 6 $MgSO_4 \cdot 7H_2O$, 0.58 $NaH_2PO_4 \cdot H_2O$, 21 $NaHCO_3$, 30 D-glucose) bubbled with 95% O_2 and 5% CO_2. To expose the spinal cords, a ventral laminectomy was performed, and they were subsequently isolated together with the ventral roots and ganglia. Spinal cords were roughly (anterior–posterior length $\times$lateral width $\times$ ventral–dorsal height) $15 \times 1 \times 1.5$ mm, increasing with days postnatal.

Prior to live spinal cord transportation, the cord was placed in a sealed 50 ml tube with 10 ml aCSF previously bubbled with 95% O_2 and 5% CO_2. The air in the tube was flushed with 95% O_2 and 5% CO_2.

For fixed experiments, at the end of dissection the cords were fixed in 4% paraformaldehyde overnight at $4°\mathrm{C}$. Fixative was then replaced with aCSF three times over the course of two days to remove any residual paraformaldehyde.

Triton X-100 (Sigma-Aldrich) nonionic surfactant was used to delipidate spinal cords. Samples (n = 2) were studied during delpidation by replacing the aCSF media with aCSF media containing a specified % of Triton X during NMR recording. Samples (n = 2) were also studied after delipidation with 10% Triton X in phosphate buffered saline (PBS) for two days, removal of Triton X by periodically replacing the PBS media for two more days, and equilibration in aCSF for a final day.

NMR hardware. NMR measurements were performed at 13.79 MHz proton frequency with a Kea2 spectrometer (Magritek, Wellington, New Zealand). A PM-10 NMR MOUSE (Magritek, Aachen, Germany) permanent magnet (45) provided a B_0 magnetic field specially designed to be constant along an x–z (10 mm $\times$ 10 mm) plane parallel to the magnet's surface and to decrease rapidly and linearly in the perpendicular (y-direction) from the surface, providing a strong static magnetic field gradient (See Fig. 9 (c)) (59).

bioRxiv preprint doi: https://doi.org/10.1101/694661; this version posted November 21, 2019. The copyright holder for this preprint (which was not certified by peer review) is the author/funder. All rights reserved. No reuse allowed without permission.

The NMR MOUSE was raised or lowered with a stepper motor with a step size of 50 μm in order to move $B_0 = 0.3239$ T, 13.79 MHz, to the precise depth within the sample (17 mm from the surface of the magnet). At this depth the magnetic field gradient g = 15.3 T/m, or 650 KHz/mm.

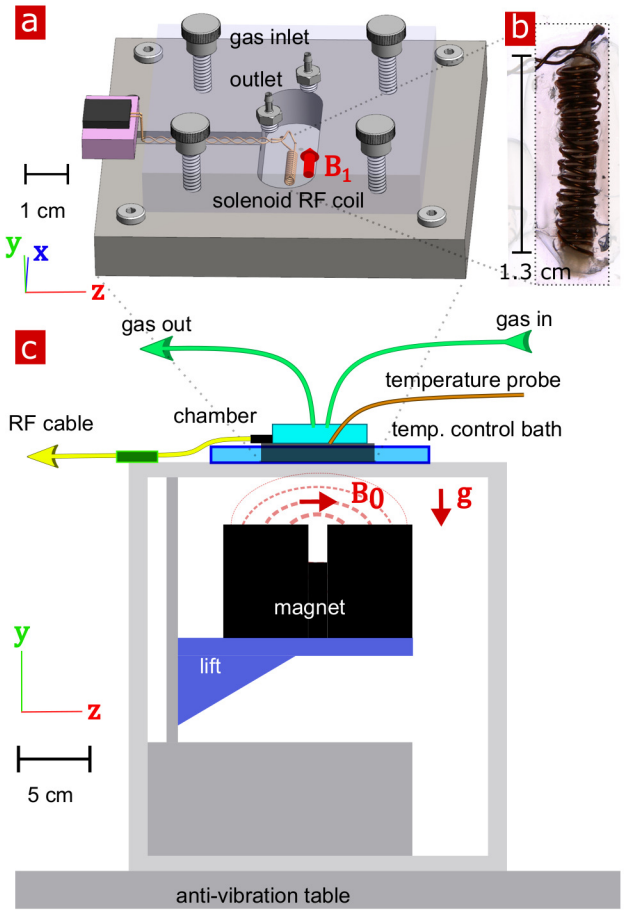

Fig. 9. Experimental setup. a) 3-D technical drawing of the test chamber. b) Image of the solenoid RF coil containing a fixed, delipidated specimen. c) Technical drawing of the experimental setup. The magnet is drawn in the "service" position to show the field lines extending from one magnetic pole to the other. To perform measurements, the magnet would be raised such that the B_0 was correctly positioned relative to the sample. Vectors B_1, g and B_0 point in the x, y, and z directions respectively

Double-wrapped (length × inner diameter) 13 × 2 mm solenoid radiofrequency (RF) coils (Fig. 9 (b)) and an RF circuit were built in-house. The solenoid connected to the circuit board with detachable pin connectors. Tune and match used two trimmer capacitors with range 1–23 pF (NMAJ25HV, Knowles Voltronics). RF pulses were driven by a 100 W RF pulse amplifier (Tomco, Adelaide, Australia). (See SI and Fig. S9 for additional information and circuit design.)

NMR experimental methods. NMR measurements were performed in Prospa 3.22 (Magritek). All measurements set repetition time (TR) = 2 s, 90°/180° pulse times = 2 μs and amplitudes = -22/-16 dB, and acquired 2000 CPMG echoes with 25 μs echo time. The acquisition time and dwell time were 4 and 0.5 μs respectively, leading to roughly a 400 μm slice thickness. The lift was positioned such that the signal was at a maximum, thus providing a slice through the center of the solenoid. Signal was phased such that the component from the real channel was maximum and the mean of the imaginary channel component was zero. Measurements were performed at room temperature or else at a controlled temperature 25 ± 0.5°C when specified in figure captions.

Diffusion measurements were performed using the spin echo sequence (49) (Fig. S10 (a)). τ was incremented linearly from 0.05 to 6.55 ms in 43 data points (corresponding to b values from 1.4 to 3,130,000 $\mathrm{s/mm^2}$) or, for live and some fixed specimen, from 0.05 to 3.3 ms in 22 points. Diffusion data is made available as supplementary material. (See SI for additional information.)

The DEXSY sequence (Fig. S10 (b)) was written in-house and used eight phase cycle steps. For full 2-D DEXSY measurements (31), data points were acquired on a 21×21 b_1, b_2 grid by incrementing τ_1 linearly from 0.200 to 3.3 ms in an inner loop and τ_2 from 0.213 to 3.313 ms in an outer loop. For the rapid exchange measurement, points were acquired as a function of b_s and b_d by varying τ_1 and τ_2 accordingly. For rapid exchange measurements (39), the standard 4-point acquisition used one point at $b_s = 200$, $b_d = 20$ $\mathrm{s/mm^2}$, and three points along $b_s = 4500$ $\mathrm{s/mm^2}$ with $b_d = -4300$, -150, and $b_d = 4300$. Unless otherwise specified, the t_m list was [0.2, 4, 20, 160] ms for full DEXSYs and [0.2, 1, 2, 4, 7, 10, 20, 40, 80, 160, 300] ms for the rapid exchange measurement. DEXSY and rapid exchange data is made available as supplementary material. The DEXSY pulse sequence can be made available upon reasonable request. (See SI and table S1 for sequence details and phase cycles.)

Standard CPMG T_2 (10 s TR, 8000 echoes) and saturation recovery T_1 (1 s TR, 21 recovery points logarithmically spaced to 10 s) measurements were performed, with all other parameters consistent with diffusion and exchange measurements. The data was fit with a monoexponential. (See Figs. S10 and S11.) The T_2/T_1 values were 275 ± 5/1870 ± 10 ms for aCSF (3 measurements), 155 ± 13/972 ± 53 ms for fixed spinal cords (n = 10/4), and 176 ± 35/1030 ms for fixed spinal cords after delipidation (n = 3/1).

NMR data analysis. 1-D distributions were fit using ℓ_2 regularization (51) and singular value decomposition (97, 98), with 50 grid points logarithmically spaced from 10^{-13} to 10^{-8} $\mathrm{m^2/s}$, and the regularization parameter chosen using the generalized cross validation (GCV) method (99). 2-D distributions were fit with an algorithm which uses ℓ_2 regularization and singular value decomposition (97, 98), with 21x21 grid points logarithmically spaced from 10^{-13} to 10^{-8} $\mathrm{m^2/s}$ and the regularization parameter chosen by the L-curve method (63) and held constant for all experiments. Exchange fractions were calculated from the rapid exchange measurement using Eqs. S8–S10 with $D_e = 10^{-9}$ and $D_i = 10^{-11}$ $\mathrm{m^2/s}$. AXRs from both full DEXSYs and the rapid exchange measurement were estimated from fits of a first order rate model, Eqs. S11–S12 (34, 39, 52), incorporating a non-zero initial condition to account for exchange during encoding (53). All analysis was performed

bioRxiv preprint doi: https://doi.org/10.1101/694661; this version posted November 21, 2019. The copyright holder for this preprint (which was not certified by peer review) is the author/funder. All rights reserved. No reuse allowed without permission.

using MATLAB (MathWorks). (See SI for additional information.)

System characteristics led to high SNR diffusion measurements. Although SNR is highly dependent on the magnetic field strength, the decrease in SNR at low field is boosted by refocussing the signal 2000 times in a CPMG train for each data point (49). Moreover, the solenoid RF coil maximized the sample filling factor, increasing SNR roughly 10-fold from previous flat RF designs (100). RF pulses used little power, permitting short 2 μs RF pulse durations and producing negligible heat. The coil design allowed for short echo times which reduced relaxation during acquisition in the CPMG train, again boosting SNR. Significant attention was given to shielding and grounding the equipment to minimize noise pickup. All together, 1-D diffusion measurements obtained SNR > 500. (See SI and Fig. S2 for additional information on noise and SNR.)

Electrophysiological recording. Electrical activity from motoneurons was recorded with suction electrodes into which individual ventral roots (L6 or T10) were drawn after NMR measurements (n = 4). The recorded signals were filtered (between 0.1 and 3 kHz) and amplified (gain: 1000), digitized at 10 kHz (Digidata 1500 B) and stored digitally on a computer. Episodes of data were analyzed off-line using MATLAB. To elicit monosynaptic responses in motoneurons, the homonymous dorsal roots were stimulated with a single electrical pulse (250 μs duration) repeated 5 times at 30 s intervals. The threshold for a given spinal root was defined as the lowest current intensity at which that root had to be stimulated to elicit a monosynaptic response in 5/5 attempts. Recordings were obtained at 5 $\times$ threshold.

Statistical analysis and reproducibility. The Results section presents data from multiple measurements repeated on individual specimen as well as measurements performed on groups of samples with different treatments (n $= x$). Each sample/specimen corresponds to one mouse spinal cord. The number of samples for each treatment group and (measurement type) were 9 / 6 / 5 / 1 / 2 / 2 for live (diffusion) / fixed (diffusion) / fixed (full DEXSY and rapid exchange) / fixed D_2O wash (diffusion and rapid exchange) / fixed delipidation timecourse (diffusion and rapid exchange) / fixed delipidated 10% Triton (diffusion) . Means and standard deviations (SD) are presented to quantify repeat measurement and sample-to-sample reproducibility of the results.

ACKNOWLEDGEMENTS

We thank Randall Pursley, Danny Trang, and Marcial Garmendia-Cedillos for electrical engineering help, Sarah Avram for Triton X delipidation protocol advice, Alexandru Avram and Miki Komlosh for general suggestions, Uzi Eliav for phase cycling expertise, Elizabeth Murphy for resource provisions, and Petrik Galvosas for the 2D inversion code. Special thanks to Velencia Witherspoon for suggesting the solenoid coil and the D_2O wash. NHW thanks attendees of the 2019 Tissue Microstructure Imaging Conference GRC for their input. NHW, DB and PJB were supported by the IRP of the NICHD, NIH. DB was also supported by the Center for Neuroscience and Regenerative Medicine, Henry Jackson Foundation, Bethesda, MD. HM, MF, MJO were funded by NINDS. DI was funded by NIMH.

Bibliography

1. Peter J Basser, James Mattiello, and Denis LeBihan. Mr diffusion tensor spectroscopy and imaging. *Biophysical journal*, 66(1):259–267, 1994.
2. Christian Beaulieu and Peter S Allen. Water diffusion in the giant axon of the squid: implications for diffusion-weighted mri of the nervous system. *Magnetic Resonance in Medicine*, 32(5):579–583, 1994.
3. Christian Beaulieu. The basis of anisotropic water diffusion in the nervous system–a technical review. *NMR in Biomedicine*, 15(7-8):435–455, 2002.
4. Kwanghun Chung, Jenelle Wallace, Sung-Yon Kim, Sandhiya Kalyanasundaram, Aaron S Andalman, Thomas J Davidson, Julie J Mirzabekov, Kelly A Zalocusky, Joanna Mattis, Aleksandra K Denisin, et al. Structural and molecular interrogation of intact biological systems. *Nature*, 497(7449):332, 2013.
5. Kazuki Tainaka, Tatsuya C Murakami, Etsuo A Susaki, Chika Shimizu, Rie Saito, Kei Takahashi, Akiko Hayashi-Takagi, Hiroshi Sekiya, Yasunobu Arima, Satoshi Nojima, et al. Chemical landscape for tissue clearing based on hydrophilic reagents. *Cell reports*, 24(8): 2196–2210, 2018.
6. Christoph Leuze, Markus Aswendt, Emily Ferenczi, Corey W Liu, Brian Hsueh, Maged Goubran, Qiyuan Tian, Gary Steinberg, Michael M Zeineh, Karl Deisseroth, et al. The separate effects of lipids and proteins on brain mri contrast revealed through tissue clearing. *Neuroimage*, 156:412–422, 2017.
7. Paul T Callaghan, Christoph H Arns, Petrik Galvosas, Mark W Hunter, Ying Qiao, and Kate E Washburn. Recent fourier and laplace perspectives for multidimensional nmr in porous media. *Magnetic resonance imaging*, 25(4):441–444, 2007.
8. Erwin L Hahn. Spin echoes. *Physical review*, 80(4):580, 1950.
9. Herman Y Carr and Edward M Purcell. Effects of diffusion on free precession in nuclear magnetic resonance experiments. *Physical review*, 94(3):630, 1954.
10. Paul T Callaghan, Andrew Coy, David MacGowan, Ken J Packer, and Fernando O Zelaya. Diffraction-like effects in nmr diffusion studies of fluids in porous solids. *Nature*, 351(6326): 467, 1991.
11. P.T. Callaghan. *Translational Dynamics and Magnetic Resonance Principles of Pulsed Gradient Spin Echo NMR*. Oxford University Press, 2011.
12. Dmitry S Novikov, Jens H Jensen, Joseph A Helpern, and Els Fieremans. Revealing mesoscopic structural universality with diffusion. *Proceedings of the National Academy of Sciences*, 111(14):5088–5093, 2014.
13. Edward O Stejskal and John E Tanner. Spin diffusion measurements: spin echoes in the presence of a time-dependent field gradient. *The journal of chemical physics*, 42(1): 288–292, 1965.
14. Donald E Woessner. Effects of diffusion in nuclear magnetic resonance spin-echo experiments. *The Journal of Chemical Physics*, 34(6):2057–2061, 1961.
15. Richard Conable Wayne and Robert M Cotts. Nuclear-magnetic-resonance study of self-diffusion in a bounded medium. *Physical Review*, 151(1):264, 1966.
16. Baldwin Robertson. Spin-echo decay of spins diffusing in a bounded region. *Physical Review*, 151(1):273, 1966.
17. CH Neuman. Spin echo of spins diffusing in a bounded medium. *The Journal of Chemical Physics*, 60(11):4508–4511, 1974.
18. Thomas M de Swiet and Pabitra N Sen. Decay of nuclear magnetization by bounded diffusion in a constant field gradient. *The Journal of chemical physics*, 100(8):5597–5604, 1994.
19. MD Hurlimann, KG Helmer, TM Deswiet, and PN Sen. Spin echoes in a constant gradient and in the presence of simple restriction. *Journal of Magnetic Resonance*, 113:260–264, 1995.
20. Dan Benjamini and Peter J Basser. Magnetic resonance microdynamic imaging reveals distinct tissue microenvironments. *NeuroImage*, 163:183–196, 2017.
21. Dmitry S Novikov, Valerij G Kiselev, and Sune N Jespersen. On modeling. *Magnetic resonance in medicine*, 79(6):3172–3193, 2018.
22. Josef Pfeuffer, Stephen W Provencher, and Rolf Gruetter. Water diffusion in rat brain in vivo as detected at very largeb values is multicompartmental. *Magnetic Resonance Materials in Physics, Biology and Medicine*, 8(2):98–108, 1999.
23. Dan Benjamini and Peter J. Basser. Water mobility spectral imaging of the spinal cord: Parametrization of model-free Laplace MRI. *Magnetic Resonance Imaging*, 56:187–193, 2019.
24. Itamar Ronen, Steen Moeller, Kamil Ugurbil, and Dae-Shik Kim. Analysis of the distribution of diffusion coefficients in cat brain at 9.4 T using the inverse Laplace transformation. *Magnetic Resonance Imaging*, 24(1):61–68, 2006.
25. Jan Andrasko. Water diffusion permeability of human erythrocytes studied by a pulsed gradient nmr technique. *Biochimica et Biophysica Acta (BBA)-General Subjects*, 428(2): 304–311, 1976.
26. JÖRG KÄRGER, Harry Pfeifer, and Wilfried Heink. Principles and application of self-diffusion measurements by nuclear magnetic resonance. In *Advances in Magnetic and optical resonance*, volume 12, pages 1–89. Elsevier, 1988.
27. A Reginald Waldeck, M Hossein Nouri-Sorkhabi, David R Sullivan, and Philip W Kuchel. Effects of cholesterol on transmembrane water diffusion in human erythrocytes measured using pulsed field gradient nmr. *Biophysical chemistry*, 55(3):197–208, 1995.
28. Josef Pfeuffer, Ulrich Flögel, Wolfgang Dreher, and Dieter Leibfritz. Restricted diffusion and exchange of intracellular water: theoretical modelling and diffusion time dependence of 1h nmr measurements on perfused glial cells. *NMR in Biomedicine: An International Journal Devoted to the Development and Application of Magnetic Resonance In Vivo*, 11 (1):19–31, 1998.
29. Peter E Thelwall, Samuel C Grant, Greg J Stanisz, and Stephen J Blackband. Human erythrocyte ghosts: exploring the origins of multiexponential water diffusion in a model biological tissue with magnetic resonance. *Magnetic Resonance in Medicine: An Official Journal of the International Society for Magnetic Resonance in Medicine*, 48(4):649–657, 2002.
30. Yuan Cheng and David G Cory. Multiple scattering by nmr. *Journal of the American Chemical Society*, 121(34):7935–7936, 1999.

bioRxiv preprint doi: https://doi.org/10.1101/694661; this version posted November 21, 2019. The copyright holder for this preprint (which was not certified by peer review) is the author/funder. All rights reserved. No reuse allowed without permission.

31. P. T. Callaghan and I. Furó. Diffusion-diffusion correlation and exchange as a signature for local order and dynamics. *The Journal of Chemical Physics*, 120(8):4032–4038, 2004.
32. Ying Qiao, Petrik Galvosas, Thorsteinn Adalsteinsson, Monika Schönhoff, and Paul T Callaghan. Diffusion exchange nmr spectroscopic study of dextran exchange through polyelectrolyte multilayer capsules. *The Journal of chemical physics*, 122(21):214912, 2005.
33. Diana Bernin and Daniel Topgaard. NMR diffusion and relaxation correlation methods: New insights in heterogeneous materials. *Current Opinion in Colloid and Interface Science*, 18(3):166–172, 2013. ISSN 1359-0294.
34. Dan Benjamini, Michal E. Komlosh, and Peter J. Basser. Imaging local diffusive dynamics using diffusion exchange spectroscopy MRI. *Physical Review Letters*, 118:158003, Apr 2017.
35. Ruiliang Bai, Dan Benjamini, Jian Cheng, and Peter J Basser. Fast, accurate 2d-mr relaxation exchange spectroscopy (rexsy): Beyond compressed sensing. *The Journal of chemical physics*, 145(15):154202, 2016.
36. Dan Benjamini and Peter J. Basser. Use of marginal distributions constrained optimization (MADCO) for accelerated 2D MRI relaxometry and diffusometry. *Journal of Magnetic Resonance*, 271:40–45, 2016. ISSN 1090-7807.
37. Dan Benjamini and Peter J. Basser. Towards clinically feasible relaxation-diffusion correlation MRI using MADCO. *Microporous and Mesoporous Materials*, 269:93–96, 2018.
38. Ingrid Åslund, Agnieszka Nowacka, Markus Nilsson, and Daniel Topgaard. Filter-exchange PGSE NMR determination of cell membrane permeability. *Journal of Magnetic Resonance*, 200(2):291 – 295, 2009. ISSN 1090-7807.
39. Teddy X Cai, Dan Benjamini, Michal E Komlosh, Peter J Basser, and Nathan H Williamson. Rapid detection of the presence of diffusion exchange. *Journal of Magnetic Resonance*, 297:17–22, 2018.
40. Samo Lasič, Markus Nilsson, Jimmy Lätt, Freddy Ståhlberg, and Daniel Topgaard. Apparent exchange rate mapping with diffusion mri. *Magnetic resonance in medicine*, 66(2): 356–365, 2011.
41. Markus Nilsson, Samo Lasič, Ivana Drobnjak, Daniel Topgaard, and Carl-Fredrik Westin. Resolution limit of cylinder diameter estimation by diffusion mri: The impact of gradient waveform and orientation dispersion. *NMR in Biomedicine*, 30(7):e3711, 2017.
42. Donghan M Yang, James E Huettner, G Larry Bretthorst, Jeffrey J Neil, Joel R Garbow, and Joseph JH Ackerman. Intracellular water preexchange lifetime in neurons and astrocytes. *Magnetic resonance in medicine*, 79(3):1616–1627, 2018.
43. William S Price. Pulsed-field gradient nuclear magnetic resonance as a tool for studying translational diffusion: Part ii. experimental aspects. *Concepts in Magnetic Resonance: An Educational Journal*, 10(4):197–237, 1998.
44. R Kimmich, W Unrath, G Schnur, and E Rommel. Nmr measurement of small self-diffusion coefficients in the fringe field of superconducting magnets. *Journal of Magnetic Resonance*, 91(1):136–140, 1991.
45. G Eidmann, R Savelsberg, Peter Blümler, and Bernhard Blümich. The nmr mouse, a mobile universal surface explorer. *Journal of Magnetic Resonance*, 122:104–109, 1996.
46. KJ Carlton, MR Halse, and John H Strange. Diffusion-weighted imaging of bacteria colonies in the strafi plane. *Journal of Magnetic Resonance*, 143(1):24–29, 2000.
47. K Potter, RL Kleinberg, FJ Brockman, and EW McFarland. Assay for bacteria in porous media by diffusion-weighted nmr. *Journal of Magnetic Resonance, Series B*, 113(1):9–15, 1996.
48. Janez Stepišnik, Carlos Mattea, Siegfried Stapf, and Aleš Mohorič. Molecular velocity auto-correlation of simple liquids observed by nmr mgse method. *The European Physical Journal B*, 91(11):293, 2018.
49. D.G. Rata, F. Casanova, J. Perlo, D.E. Demco, and B. Blümich. Self-diffusion measurements by a mobile single-sided nmr sensor with improved magnetic field gradient. *Journal of Magnetic Resonance*, 180(2):229 – 235, 2006. ISSN 1090-7807. doi: https://doi.org/10.1016/j.jmr.2006.02.015.
50. Oliver Neudert, Siegfried Stapf, and Carlos Mattea. Diffusion exchange nmr spectroscopy in inhomogeneous magnetic fields. *Journal of Magnetic Resonance*, 208(2):256–261, 2011.
51. Stephen W. Provencher. A constrained regularization method for inverting data represented by linear algebraic or integral equations. *Computer Physics Communications*, 27 (3):213–227, 1982.
52. K. E. Washburn and P. T. Callaghan. Tracking pore to pore exchange using relaxation exchange spectroscopy. *Physical Review Letters*, 97:175502, Oct 2006.
53. Nathan H Williamson, April M Dower, Sarah L Codd, Amber L Broadbent, Dieter Gross, and Joseph D Seymour. Glass dynamics and domain size in a solvent-polymer weak gel measured by multidimensional magnetic resonance relaxometry and diffusometry. *Physical review letters*, 122(6):068001, 2019.
54. RD Dortch, RA Horch, and MD Does. Development, simulation, and validation of NMR relaxation-based exchange measurements. *The Journal of Chemical Physics*, 131(16): 164502, 2009.
55. Maxime Van Landeghem, Agnes Haber, Jean-Baptiste D'espinose De Lacaillerie, and Bernhard Blümich. Analysis of multisite 2d relaxation exchange nmr. *Concepts in Magnetic Resonance Part A*, 36(3):153–169, 2010.
56. Ruobing Song, Yi-Qiao Song, Muthusamy Vembusubramanian, and Jeffrey L. Paulsen. The robust identification of exchange from t2–t2 time-domain features. *Journal of Magnetic Resonance*, 265:164 – 171, 2016. ISSN 1090-7807.
57. CLG Ham, JML Engels, GT Van de Wiel, and A Machielsen. Peripheral nerve stimulation during mri: effects of high gradient amplitudes and switching rates. *Journal of Magnetic Resonance Imaging*, 7(5):933–937, 1997.
58. M Köpf, C Corinth, O Haferkamp, and TF Nonnenmacher. Anomalous diffusion of water in biological tissues. *Biophysical journal*, 70(6):2950–2958, 1996.
59. J Perlo, F Casanova, and B Blümich. Profiles with microscopic resolution by single-sided nmr. *Journal of magnetic resonance*, 176(1):64–70, 2005.
60. Federico Casanova, Juan Perlo, and Bernhard Blümich. *Single-sided NMR*. Springer, 2011.
61. Ernesto Danieli and Bernhard Blümich. Single-sided magnetic resonance profiling in biological and materials science. *Journal of Magnetic Resonance*, 229:142–154, 2013.
62. Christian Rehorn and Bernhard Blümich. Cultural heritage studies with mobile nmr. *Angewandte Chemie International Edition*, 57(25):7304–7312, 2018.
63. J Mitchell, TC Chandrasekera, and LF Gladden. Numerical estimation of relaxation and diffusion distributions in two dimensions. *Progress in nuclear magnetic resonance spectroscopy*, 62:34–50, 2012.
64. Daniel Nunes, Andrada Ianus, and Noam Shemesh. Layer-specific connectivity revealed by diffusion-weighted functional mri in the rat thalamocortical pathway. *NeuroImage*, 184: 646–657, 2019.
65. David L Buckley, Jonathan D Bui, M Ian Phillips, Tibor Zelles, Benjamin A Inglis, H Daniel Plant, and Stephen J Blackband. The effect of ouabain on water diffusion in the rat hippocampal slice measured by high resolution nmr imaging. *Magnetic Resonance in Medicine: An Official Journal of the International Society for Magnetic Resonance in Medicine*, 41(1):137–142, 1999.
66. JD Bui, DL Buckley, MI Phillips, and SJ Blackband. Nuclear magnetic resonance imaging measurements of water diffusion in the perfused hippocampal slice during n-methyl-d-aspartate-induced excitotoxicity. *Neuroscience*, 93(2):487–490, 1999.
67. Timothy M Shepherd, Stephen J Blackband, and Edward D Wirth III. Simultaneous diffusion mri measurements from multiple perfused rat hippocampal slices. *Magnetic Resonance in Medicine: An Official Journal of the International Society for Magnetic Resonance in Medicine*, 48(3):565–569, 2002.
68. Timothy M Shepherd, Peter E Thelwall, Greg J Stanisz, and Stephen J Blackband. Aldehyde fixative solutions alter the water relaxation and diffusion properties of nervous tissue. *Magnetic Resonance in Medicine: An Official Journal of the International Society for Magnetic Resonance in Medicine*, 62(1):26–34, 2009.
69. Nitzan Tirosh and Uri Nevo. Neuronal activity significantly reduces water displacement: Dwi of a vital rat spinal cord with no hemodynamic effect. *Neuroimage*, 76:98–107, 2013.
70. Ruiliang Bai, Craig V Stewart, Dietmar Plenz, and Peter J Basser. Assessing the sensitivity of diffusion mri to detect neuronal activity directly. *Proceedings of the National Academy of Sciences*, 113(12):E1728–E1737, 2016.
71. Hilary T Fabich, Partha Nandi, Hans Thomann, and Mark S Conradi. Diffusion measurements using the second echo. *Concepts in Magnetic Resonance Part A*, 47(2):e21462, 2018.
72. Barbara P Fulton. Motoneurone activity in an isolated spinal cord preparation from the adult mouse. *Neuroscience letters*, 71(2):175–180, 1986.
73. RJA Wilson, T Chersa, and PJ Whelan. Tissue po2 and the effects of hypoxia on the generation of locomotor-like activity in the in vitro spinal cord of the neonatal mouse. *Neuroscience*, 117(1):183–196, 2003.
74. Sarah E Mailhiot, Nathan H Williamson, Jennifer R Brown, Joseph D Seymour, Sarah L Codd, and Ronald K June. $t_1 - t_2$ correlation and biopolymer diffusion within human osteoarthritic cartilage measured with nuclear magnetic resonance. *Applied Magnetic Resonance*, 48(4):407–422, 2017.
75. Denis S Grebenkov. Diffusion mri/nmr at high gradients: Challenges and perspectives. *Microporous and Mesoporous Materials*, 269:79–82, 2018.
76. Nathan H Williamson, Magnus Nydén, and Magnus Röding. The lognormal and gamma distribution models for estimating molecular weight distributions of polymers using pgse nmr. *Journal of Magnetic Resonance*, 267:54–62, 2016.
77. L Masaro and XX Zhu. Physical models of diffusion for polymer solutions, gels and solids. *Progress in polymer science*, 24(5):731–775, 1999.
78. Lawrence L Latour, Karel Svoboda, Partha P Mitra, and Christopher H Sotak. Time-dependent diffusion of water in a biological model system. *Proceedings of the National Academy of Sciences*, 91(4):1229–1233, 1994.
79. Alex M Henry and John G Hohmann. High-resolution gene expression atlases for adult and developing mouse brain and spinal cord. *Mammalian genome*, 23(9-10):539–549, 2012.
80. Gulgun Sengul, Ralph B Puchalski, and Charles Watson. Cytoarchitecture of the spinal cord of the postnatal (p4) mouse. *The Anatomical Record: Advances in Integrative Anatomy and Evolutionary Biology*, 295(5):837–845, 2012.
81. Eric R Kandel, James H Schwartz, Thomas M Jessell, Department of Biochemistry, Molecular Biophysics Thomas Jessell, Steven Siegelbaum, and AJ Hudspeth. *Principles of neural science*, volume 5. McGraw-hill New York, 2013.
82. Justin P Kinney, Josef Spacek, Thomas M Bartol, Chandrajit L Bajaj, Kristen M Harris, and Terrence J Sejnowski. Extracellular sheets and tunnels modulate glutamate diffusion in hippocampal neuropil. *Journal of Comparative Neurology*, 521(2):448–464, 2013.
83. Denis S Grebenkov. NMR survey of reflected brownian motion. *Reviews of Modern Physics*, 79(3):1077, 2007.
84. Nicolas Moutal, Kerstin Demberg, Denis S. Grebenkov, and Tristan Anselm Kuder. Localization regime in diffusion nmr: Theory and experiments. *Journal of Magnetic Resonance*, 305:162 – 174, 2019. ISSN 1090-7807. doi: https://doi.org/10.1016/j.jmr.2019.06.016.
85. Peter J. Basser and Carlo Pierpaoli. Microstructural and physiological features of tissues elucidated by quantitative-diffusion-tensor mri. *Journal of Magnetic Resonance, Series B*, 111(3):209 – 219, 1996. ISSN 1064-1866. doi: https://doi.org/10.1006/jmrb.1996.0086.
86. ME Komlosh, F Horkay, RZ Freidlin, U Nevo, Yaniv Assaf, and PJ Basser. Detection of microscopic anisotropy in gray matter and in a novel tissue phantom using double pulsed gradient spin echo mr. *Journal of magnetic resonance*, 189(1):38–45, 2007.
87. Dan Benjamini, Jonathan J. Elsner, Meital Zilberman, and Uri Nevo. Pore size distribution of bioresorbable films using a 3-D diffusion NMR method. *Acta Biomaterialia*, 10:2762–2768, 2014.
88. Dan Benjamini, Michal E. Komlosh, Lynne A. Holtzclaw, Uri Nevo, and Peter J. Basser. White matter microstructure from nonparametric axon diameter distribution mapping. *NeuroImage*, 135:333 – 344, 2016. ISSN 1053-8119.
89. James D Quirk, G Larry Bretthorst, Timothy Q Duong, Avi Z Snyder, Charles S Springer Jr, Joseph JH Ackerman, and Jeffrey J Neil. Equilibrium water exchange between the intra- and extracellular spaces of mammalian brain. *Magnetic Resonance in Medicine: An Official Journal of the International Society for Magnetic Resonance in Medicine*, 50(3):493–499, 2003.
90. Markus Nilsson, Jimmy Lätt, Danielle van Westen, Sara Brockstedt, Samo Lasič, Freddy

bioRxiv preprint doi: https://doi.org/10.1101/694661; this version posted November 21, 2019. The copyright holder for this preprint (which was not certified by peer review) is the author/funder. All rights reserved. No reuse allowed without permission.

Ståhlberg, and Daniel Topgaard. Noninvasive mapping of water diffusional exchange in the human brain using filter-exchange imaging. *Magnetic Resonance in Medicine*, 69(6): 1572–1580, 2013.

91. Ruiliang Bai, Charles S Springer Jr, Dietmar Plenz, and Peter J Basser. Fast, na+/k+ pump driven, steady-state transcytolemmal water exchange in neuronal tissue: A study of rat brain cortical cultures. *Magnetic Resonance in Medicine*, 79(6):3207–3217, 2018.
92. Ruiliang Bai, Charles S Springer Jr, Dietmar Plenz, and Peter J Basser. Brain active transmembrane water cycling measured by mr is associated with neuronal activity. *Magnetic resonance in medicine*, 81(2):1280–1295, 2019.
93. Philip W Kuchel and Gheorghe Benga. Why does the mammalian red blood cell have aquaporins? *Biosystems*, 82(2):189–196, 2005.
94. J Veraart, E Fieremans, U Rudrapatna, D Jones, and DS Novikov. Biophysical modeling of the gray matter: does the "stick" model hold. In *Proceedings of the 27th Annual Meeting of ISMRM, Paris, France*, 2018.
95. Yaniv Assaf, Tamar Blumenfeld-Katzir, Yossi Yovel, and Peter J Basser. Axcaliber: a method for measuring axon diameter distribution from diffusion mri. *Magnetic Resonance in Medicine: An Official Journal of the International Society for Magnetic Resonance in Medicine*, 59(6):1347–1354, 2008.
96. Yaniv Assaf and Yoram Cohen. Assignment of the water slow-diffusing component in the central nervous system using q-space diffusion mrs: implications for fiber tract imaging. *Magnetic Resonance in Medicine: An Official Journal of the International Society for Magnetic Resonance in Medicine*, 43(2):191–199, 2000.
97. L. Venkataramanan, Yi-Qiao Song, and Martin D. Hürlimann. Solving Fredholm integrals of the first kind with tensor product structure in 2 and 2.5 dimensions. *IEEE Trans. Signal. Process.*, 50(5):1017–1026, 2002. ISSN 1053-587X.
98. S Godefroy and PT Callaghan. 2d relaxation/diffusion correlations in porous media. *Magnetic Resonance Imaging*, 21(3-4):381–383, 2003.
99. Gene H. Golub, Michael Heath, and Grace Wahba. Generalized Cross-Validation as a Method for Choosing a Good Ridge Parameter. *Technometrics*, 21(2):215, 1979.
100. Ruiliang Bai, Andreas Klaus, Tim Bellay, Craig Stewart, Sinisa Pajevic, Uri Nevo, Hellmut Merkle, Dietmar Plenz, and Peter J Basser. Simultaneous calcium fluorescence imaging and mr of ex vivo organotypic cortical cultures: a new test bed for functional mri. *NMR in Biomedicine*, 28(12):1726–1738, 2015.

bioRxiv preprint doi: https://doi.org/10.1101/694661; this version posted November 21, 2019. The copyright holder for this preprint (which was not certified by peer review) is the author/funder. All rights reserved. No reuse allowed without permission.

Supplementary theory

Diffusion signal attenuation models. Attenuation of the MR signal in a spin echo diffusion experiment under a static magnetic field gradient can exhibit three diffusion regimes corresponding to three different characteristic length scales: the restriction length l_s, the diffusion length, $l_d = \sqrt{D_0\tau}$, and the dephasing length, $l_g = (D_0/\gamma g)^{1/3}$ where $D_0 = 2.15\ \mathrm{m}^2/\mathrm{s}$ is the diffusion coefficient of water in artificial cerebro-spinal fluid (aCSF) at 25°C, τ is the time between the first 90° and the 180° radio frequency refocussing pulses of the spin echo sequence or $1/2$ the echo time TE, and γ is the gyromagnetic ratio (1). The diffusion length is the average distance that water diffuses during the time τ. In the spin echo diffusion measurements, τ was linearly increased from 0.05 to 3.3 or to 6.6 ms, corresponding to $l_D = 0.33$, 2.7, and 3.7 μm respectively. The dephasing length is the distance that diffusing spins dephase by 2π radians in a spin echo measurement with a static gradient. For the 15.3 T/m gradient used here, $l_g = 800$ nm. The shortest of these three length scales determines the regime that applies to the diffusing spins, and thus dictates the asymptotic behavior of the spin echo decay. What follows is a basic interpretation of the attenuation regimes, as taken from Hürlimann, et al., (1). A complete discussion of the regimes, higher order terms to the attenuation, and a historical account of the field was provided by Grebenkov (2).

Free diffusion regime. The free diffusion regime occurs when l_D is the shortest characteristic length scale. This regime was first described by Hahn (3) and then the diffusion coefficient of water was measured by Carr and Purcell (4), both using static magnetic field gradients. In this regime, the signal decays by (5)

$$\begin{aligned} I(\tau)/I_0 &= \exp\left(-\frac{2}{3}D_0\gamma^2 g^2\tau^3\right) \\ &= \exp\left(-\frac{2}{3}\left(\frac{l_D}{l_g}\right)^6\right) \\ &= \exp\left(-bD_0\right). \end{aligned} \tag{S1}$$

Water diffusion is often modeled as Gaussian with an effective or apparent diffusion coefficient D, rather than D_0, and in the limit of low attenuation $D = \langle D\rangle$. "Apparent" implies that the measured diffusion coefficient will depend on the experimental parameters (6). This is particularly true when using Eq. S1 to model signal which includes water in other regimes. The use of b coefficient or factor comes from diffusion MRI literature (7).

Localization regime. The localization regime occurs when l_g is the shortest characteristic length scale. In this regime, signal near the restrictive surfaces will dephase more slowly than signal farther away. While the entire decay curve can be quite complicated (8), in the asymptotic long-time (τ) limit the signal was experimentally characterized by Hürlimann et al. (1) and theoretically modeled by Stoller, et al. (9), and de Swiet et al. (10), and shown to attenuate as

$$\begin{aligned} I(\tau)/I_0 &= c\frac{D_0^{1/3}}{\gamma^{1/3}g^{1/3}l_s}\exp\left(-a_1 D_0^{1/3}\gamma^{2/3}g^{2/3}\tau\right) \\ &= c\frac{l_g}{l_s}\exp\left(-a_1\left(\frac{l_D}{l_g}\right)^2\right), \end{aligned} \tag{S2}$$

where $a_1 = 1.0188$ and is, importantly, independent of the confining geometry (8). The prefactor c varies depending on the geometry and equals 5.8841 for water restricted between parallel plates (10). Higher order terms, shown in Ref. (8) do depend on geometry of the confining surface, in particular the curvature, permeability, and surface relaxivity. Note that l_s affects the fraction of signal present in the asymptotic limit but does not affect the decay. By varying τ under a static gradient, we see that the signal attenuates exponentially with τ, $(l_D/l_g)^2$ or $(bD_0)^{1/3}$.

Motional averaging regime. The motional averaging regime occurs when l_s is the shortest characteristic length scale. Signal attenuates very slowly and water can diffuse across the restricted volume many times before dephasing appreciably. Signal decay in the motional averaging regime was first experimentally measured by Wayne and Cotts (11) and subsequently modeled by Robertson (12). Neuman derived the signal attenuation models for water restricted between parallel plates and within cylinders oriented perpendicular to g, and within spheres (13). We focus on the model for spheres of radius R for which the signal attenuates by

$$I(\tau)/I_0 = \exp\left(-\frac{2\gamma^2 g^2}{D_0}\sum_{m=1}^{\infty}\frac{\alpha_m^{-4}}{\alpha_m^2R^2-2}\left(2\tau - \frac{3-4\exp(-\alpha_m^2D_0\tau)+\exp(-\alpha_m^2D_0\,2\tau)}{\alpha_m^2D_0}\right)\right) \tag{S3}$$

where α_m is the mth root of

$$\alpha_m R J'_{3/2}(\alpha_m R) - \frac{1}{2}J_{3/2}(\alpha_m R) = 0 \tag{S4}$$

bioRxiv preprint doi: https://doi.org/10.1101/694661; this version posted November 21, 2019. The copyright holder for this preprint (which was not certified by peer review) is the author/funder. All rights reserved. No reuse allowed without permission.

for which the first 5 roots are $\alpha_m R = 2.0815$, 5.940, 9.206, 12.405, and 15.579 (14). In the limit of long τ relative to the timescale to diffuse across the restriction, Eq. S3 becomes

$$\begin{aligned} I(\tau)/I_0 &= \exp\left(-\frac{8}{175}\frac{R^4\gamma^2 g^2}{D_0}\left(2\tau - \frac{581}{840}\frac{R^2}{D_0}\right)\right) \\ &\approx \exp\left(-\frac{4}{175}\left(\frac{l_D}{l_g}\right)^2\left(\frac{l_s}{l_g}\right)^4\right) \end{aligned} \tag{S5}$$

where the final approximation drops the $581/840R^2/D_0$ as insignificant. In the long-time limit, decay models for other geometries vary from Eq. S5 by a scaling within the exponential, e.g., rather than 8/175 for spheres, the scaling factor is 1/120 for parallel plates, and 7/296 for cylinders (13).

As in the long-time limit of the localization regime, decay of signal in the motional averaging regime is exponential with τ, $(l_D/l_g)^2$ or $(bD_0)^{1/3}$. Exchange also occurs on the timescale of τ and can be incorporated into the decay model by multiplying by $\exp(-2\tau\mathrm{AXR})$ where AXR is the apparent exchange rate (14).

The effect of motional averaging can be reached in the extreme case of when δ approaches Δ in pulsed gradient measurements, which researchers have commented leads to restrictions appearing smaller than they actually are (15–17). Given the gradient strength limitations on human MRI scanners, the clinical translation of advanced diffusion MRI methods requires the use of gradient pulses with maximum amplitude for efficient diffusion encoding (18). Consequently, clinical implementations of many advanced diffusion MRI preparations can be adjusted to effectively resemble/be equivalent to experiments in a static gradient field.

Decay models for the various regimes are compared in Fig. 5 of the main manuscript.

Supplementary results

Penetration timescales. The methods were used to follow penetration of deuterated water D_2O into the tissue as well as the delipidation of the tissue via Triton X. For the D_2O wash (Fig. S6), I_0 decreased to 0.36 two minutes after washing, indicating that water in the tissue communicates with the aCSF on timescales of minutes. Exchange and restricted fractions decreased during delipidation on the timescale of roughly one day (Fig. S7). Mass transport theory estimates the timescale to equilibrate a concentration gradient across the tissue as ≈ 1 min for water and ≈ 3 hrs for Triton X based on $t = r^2/4D$ (19) with specimen radius $r = 0.7$ mm and measured $D = 2.15\times10^{-9}$ $\mathrm{m^2/s}$ for water and $D = 1.3\times10^{-11}$ $\mathrm{m^2/s}$ for Triton X (see supplementary Fig. S8). The timescale of water penetration was consistent with mass transport theory (19), but the timescale of Triton X penetration and delipidation was longer than predicted. An increased time is expected due to the reaction front which develops as Triton X delipidates, slowing its overall penetration.

Testing the rapid exchange measurement on fixed spinal cord tissue. Given that this is the first time the rapid exchange measurement has been used with a static gradient as well as on anything other than an ideal phantom, a full characterization of the signal seemed necessary. Details of the rapid exchange measurement method can be found in Cai, et al., 2018 (20), and the supplementary methods section (below). In this section we test the behavior of the signal acquired as a function of b_d, b_s, and t_m on fixed spinal cord and compare results to the predicted exchange behavior (20).

The curvature along slices of $b_s = 4500$ $\mathrm{s/mm^2}$ as a function of b_d at different mixing times is shown in Fig. S13. The signal is concave up with maximum at $b_d = \pm4500$, minimum at $b_d = 0$, and roughly symmetric about $b_d = 0$, as expected. Exchange increases with mixing time, also as expected. From this, we can conclude that the 4-point method (discussed below) can capture the exchange with maximal sensitivity.

The optimal b_s maximizes the finite difference (Eq. S8) and provides optimal sensitivity to exchange in the presence of noise. However, different b_s values may diffusion-weight the measurement towards exchange between different pools. Fig. S14 shows that the finite difference reaches a maximum near $b_s = 6000$ $\mathrm{s/mm^2}$. The value $b_d = 4500$ $\mathrm{s/mm^2}$ used in this study is thus near the optimum. Additionally, from this data it was found that the exchange rate is not significantly different between b_s values, indicating that AXR is not very sensitive to b_s.

The four-point method allowed for high temporal resolution of exchange. Fig. S15 shows a dense sampling of f as a function of t_m, acquired overnight on a fixed spinal cord specimen. The data shows the $t_m = 0.1$ ms point to be not well behaved, with f decreasing from $t_m = 0.1$ to 0.2 ms, but increases from $t_m = 0.2$ ms onwards, indicating that $t_m = 0.2$ is a good point for the minimum t_m. The exchange plateaus near $t_m = 100$ ms and stays roughly constant to $t_m = 300$ ms, indicating that $t_m = 300$ ms is a good point for the maximum t_m because it captures the maximum, steady state exchange, and it does not show T_1 relaxation effects (in particular due to differences in T_1 between exchanging pools (20)). The data was fit with the first order rate model, Eq. S12, to estimate AXR. The dense sampling shows that the data is not fully explained by the first order rate model; it rises up quicker and plateaus slower. However, rather than fitting a model with more parameters, e.g. a model with two AXRs, we choose to stick to the first order rate model with one AXR. The estimated $\mathrm{AXR} = 113.7 \pm 5.2$ s^{-1}

bioRxiv preprint doi: https://doi.org/10.1101/694661; this version posted November 21, 2019. The copyright holder for this preprint (which was not certified by peer review) is the author/funder. All rights reserved. No reuse allowed without permission.

is not statistically different from the values measured from the AXR measured from the standard 11 t_m point protocol used throughout the text, indicating that the 11 point protocol does not bias the measured AXR. The dense sampling also iterates $f(t_m = 0) \neq 0$, thus calling for a non-zero initial condition (discussed below).

Supplementary materials and methods

Test chamber. The bottom portion of the experimental test chamber was made of aluminum to provide good heat conduction to the media. A bored-out rectangular hole with a glass cover slide glued to the bottom held the media, solenoid, and spinal cord. Aluminum parts that contacted aCSF were coated with a thin layer of RTV silicone to avoid corrosion. The top of the chamber was made from poly(methyl methacrylate) (PMMA) with two inlets for inflow and outflow of the gas and a hole for the PicoM fiber optic temperature sensor (Opsens Solutions Inc., Québec, Canada). Temperature measurements were not affected by RF and did not induce noise in the RF system. The temperature of the bath was monitored and recorded continuously. The top slide was secured and mounted to the bottom part with four screws. The NMR solenoid coil was glued to the glass cover slip bottom with a hot glue gun. Two separate chambers and solenoid coils were built for live and fixed spinal cord specimen.

NMR hardware. The solenoid radiofrequency (RF) coils and the circuit were built in-house. Solenoids were made from wrapping two concentric layers of AWG 30 copper wire around a #2-56 plastic screw totaling 39 turns resulting in 2 mm inner diameter 4 mm outer diameter, 1.3 cm length. The resulting coils had an inductance L $\sim$ 600 nH and impedance X $\sim$ 52 Ω at 13.79 MHz.
The solenoid connected to a circuit board with detachable pin connectors. (The circuit design is shown in Fig. S9.) The circuit used two trimmer capacitors (NMAJ25HV, Knowles Voltronics) with tunable range 1–23 pF for tune and match. The circuit board was connected to the Kea2 spectrometer by a 50 Ω coax cable. The coil matched to -34 dB at 13.79 MHz when immersed in aCSF. RF pulses were driven by a 100 W RF pulse amplifier (Tomco, Adelaide, Australia).

Noise and SNR. The noise is quantified by the standard deviation of measured output from the real channel from the standard diffusion measurement protocol defined in the Methods section (2 s TR, 2000 echoes, 4 scans, etc.), normalized by the average signal with no diffusion weighting ($\mathrm{SD}(I(\tau))/\mathrm{mean}(I_0)$). Signal-to-noise is defined as the inverse of the noise statistic (SNR $= \mathrm{mean}(I_0)/\mathrm{SD}(I(\tau))$). Fig. S2 explores noise and SNR from the standpoint of repeatability of measurements performed on a specimen over the course of 2 days, the standard deviation of noise from measurements on aCSF after aCSF signal has attenuated, and system noise on an empty coil in a dry chamber. SD of repeat measurements on a spinal cord appears similar to the SD of the noise from measurements on aCSF. The signal-to-noise ratio of the system based on diffusion measurements on aCSF is $SNR = I_0/SD = 500$. The theoretical maximum SNR is SNR=1000 based on the SD of the noise from a dry empty chamber with the circuit tuned on resonance and I_0 defined by the aCSF experiment. Anderson–Darling tests indicate that the histograms from repeat measurements are not dissimilar from Gaussian distribution (accepting the null hypothesis with $P = 0.18 > 0.05$ for the spinal cord data in (b), $P = 0.08 > 0.05$ for the aCSF data in (c), and $P = 0.54 > 0.05$ for the empty chamber data in (d). In the case of aCSF, the noise has a non-zero mean (0.0011) indicating a 0.1% noise floor, however the empty dry chamber shows zero mean noise, indicating that the noise floor from aCSF may be signal measured from an immobile component (e.g., glue or a coating on the RF coil).

1-D spin echo diffusion. A standard pulse sequence (SEdec in Prospa) was used for measuring diffusion with a static gradient (21) built off of a spin echo followed by a Carr–Purcell–Meiboom–Gill (CPMG) echo train (3, 4, 22), as shown in Fig. S10a. The phase cycle list was four scans long (23).
Signal from the CPMG train is summed up as one data point. This summation provides a significant boost in the signal-to-noise ratio (SNR). Only signal from the real channel (rather than signal magnitude) is taken. This leads to zero-mean Gaussian rather than Rician noise, a significant benefit for multiexponential signal analysis. The echo time of the spin echo τ is incremented in successive loops of the experiment to encode for diffusion. For water and with large gradient the attenuation due to T_2 relaxation during τ is insignificant. Signal can be modeled using Eq. S1 for pure liquids such as water. In heterogeneous materials such as biological tissue, water in different parts of the material experience different hindrances and restrictions. Each sub-ensemble of water molecules has its own effective self-diffusion coefficients. The signal can be modeled as arising from the distribution of effective or apparent self-diffusion coefficients of the water in the different environments using

$$I(b)/I_0 = \int_0^\infty P(D)e^{-bD}dD. \tag{S6}$$

DEXSY pulse sequence. Fig. S10b shows the static gradient spin echo DEXSY pulse sequence. In this sequence, molecules are encoded for their diffusion coefficient in their local environment during the first interval τ_1. Magnetization is then stored for a mixing time, t_m during which time molecules move freely and may exchange between diffusive environments. (Note that this definition of t_m is like the definition used for T_2–T_2 (24), and is different from the original definition presented by Callaghan and Furó which included the gradient pulse duration (25). We choose not to use that definition since τ is changing in a static

bioRxiv preprint doi: https://doi.org/10.1101/694661; this version posted November 21, 2019. The copyright holder for this preprint (which was not certified by peer review) is the author/funder. All rights reserved. No reuse allowed without permission.

gradient spin echo DEXSY measurement whereas the definition of t_m should require that it be constant throughout the whole experiment.) Molecules are again encoded for diffusion during τ_2 and then signal is acquired in a CPMG train.

Full DEXSY. The full 2-D DEXSY can be analyzed as a diffusion exchange distribution, related to the signal through

$$I(b_1,b_2) = \int_0^\infty \int_0^\infty P(D_1,D_2)e^{-b_1D_1-b_2D_2}dD_1dD_2, \tag{S7}$$

a 2-D version of Eq. S6. The diffusion encoding variables, b_1 and b_2 are varied by independently varying τ_1 and τ_2. Molecules which do not exchange between environments will have the same diffusion coefficient during τ_1 and τ_2 contributing to populations on the diagonal of the 2-D distribution (see, e.g., Fig. 2a and b in (20)). Molecules which do exchange and thus are encoded with different diffusion coefficients between the two τ will contribute to off-diagonal exchange peaks in the 2-D distribution.

Rapid exchange measurement. Alternatively to the full DEXSY, we recently introduced a rapid method for measuring exchanging fractions which relied on curvature of the raw signal after a variable transformation (26). In particular, this method shows that exchange between diffusion environments results in the raw data being curved up along a slice of constant $b_s = b_1 + b_2$ (see Fig. 2c and d in (20)). The exchanging fraction scales with $(\partial^2 I/\partial b_d^2)$ where $b_d = b_2 - b_1$. The second derivative can be approximated with the 2nd order finite difference method,

$$\frac{\partial^2 I}{\partial b_d^2}\Big|_{b_d=b} \approx \frac{I\Big|_{b_d=b-\Delta b_d} - 2I\Big|_{b_d=b} + I\Big|_{b_d=b+\Delta b_d}}{\Delta b_d^2}, \tag{S8}$$

omitting higher order terms. The greatest sensitivity to exchange is when the central point is acquired at $b_d = 0$ and the edges are acquired at $b_d = \pm b_s$. Normalizing by a datapoint acquired with no diffusion weighting $b_s = 0$ removes relaxation effects. This is a relative measure of exchange and is enough to provide image contrast in MRI, to look at time-varying processes, or to measure exchange rates (discussed below).

In our previous publication we developed the theory for obtaining the exchanging fraction, f, from $(\partial^2 I/\partial b_d^2)$, which for a two-site exchange model results in (20)

$$\begin{aligned} f &= \left(\frac{\partial^2 I}{\partial b_d^2}\Big|_{b_d=b}\right)\frac{e^{b_sD_s}}{\cosh(b_dD_d)D_d^2} \\ &= \left(\frac{\partial^2 I}{\partial b_d^2}\Big|_{b_d=0}\right)\frac{e^{b_sD_s}}{D_d^2} \end{aligned} \tag{S9}$$

where

$$D_s = \frac{(D_e + D_i)}{2};\ D_d = \frac{(D_e - D_i)}{2}. \tag{S10}$$

DEXSY sequence phase cycles. Attention was paid to phase cycles for the static gradient spin echo DEXSY sequence (Figure S10) due to each RF pulse being imperfect and exciting multiple coherence pathways when the inhomogeneity of the magnetic field is greater than the bandwidth of the RF pulses (27). The phase cycle list was eight scans long, shown in Table S1.

Table S1. DEXSY Phase Cycles

ϕ_1	ϕ_2	ϕ_3	ϕ_4	ϕ_5	ϕ_6	ϕ_{rec}
0	$+\pi/2$	0	0	$+\pi/2$	$\pi/2$	π
π	$-\pi/2$	0	0	$+\pi/2$	$\pi/2$	0
0	$+\pi/2$	π	0	$+\pi/2$	$\pi/2$	0
π	$-\pi/2$	π	0	$+\pi/2$	$\pi/2$	π
0	$+\pi/2$	0	π	$-\pi/2$	$\pi/2$	0
π	$-\pi/2$	0	π	$-\pi/2$	$\pi/2$	π
0	$+\pi/2$	π	π	$-\pi/2$	$\pi/2$	π
π	$-\pi/2$	π	π	$-\pi/2$	$\pi/2$	0

Although the phase cycle list is not exhaustive, we found the signal to be well-behaved on a non-exchanging two-pool system comprised of a capillary filled with polydymethylsyloxane bathed in water. Signal as a function of b_1 or b_2 were symmetric and decayed the same as signal as a function of b from the 1-D SEdec sequence. Additionally, signal was flat along slices

bioRxiv preprint doi: https://doi.org/10.1101/694661; this version posted November 21, 2019. The copyright holder for this preprint (which was not certified by peer review) is the author/funder. All rights reserved. No reuse allowed without permission.

of constant b_s and the 2-D DEXSY map showed two diffusion coefficients along the $D_1 = D_2$ diagonal equal to D_{water} and D_{PDMS}. One exception was that the phase cycles let through signals which do not form a gradient echo when they see the storage pulse, but do form a gradient echo upon acquisition, thus seeing the sequence as a 1-D stimulated echo diffusion. This became apparent due to additional refocussing when $b_1 = b_2$. This was found to be an issue with a previous miniature flat RF coil design (28) but went away when switching to the solenoid RF coil, thus it is likely an issue of B_1 inhomogeneity of the miniature flat RF coil (29). To avoid refocussing this signal, points were never acquired exactly on $b_1 = b_2$. Also note that the static gradient acts as a crusher during the storage interval. The sequence selects both compensated and uncompensated signals (30). The sequence can be compared and contrasted to another DEXSY sequence developed for static gradients but using stimulated echoes for diffusion encoding (31)

Fitting exchange parameters. Exchange rates can be estimated from the full DEXSY or the rapid measurement by repeating the measurement with multiple mixing times which span the exchange process. Exchange parameters can be determined assuming exchange between diffusion environments is governed by a first order rate law of the form $df_{i,e}/dt = k_{i,e} f_{i,i} - k_{e,i} f_{e,i}$ with rate constants $k_{i,e}$ and $k_{e,i}$ (24). The data we present calls for a nonzero initial condition; $f_{i,e}(t_m = 0) = f_{i,e0}$ (discussed below). The resulting two-site exchange model is:

$$\begin{aligned} f_{i,e}(t) = f_{e,i}(t) = \frac{f(t)}{2} &= \left(\frac{f_e k_{e,i}}{k_{e,i} + k_{i,e}} - f_{e,i0} \right) \left(1 - e^{-(k_{i,e}+k_{e,i})t} \right) + f_{e,i0} \\ &= \left(\frac{f_i k_{i,e}}{k_{i,e} + k_{e,i}} - f_{i,e0} \right) \left(1 - e^{-(k_{e,i}+k_{i,e})t} \right) + f_{i,e0}, \end{aligned} \tag{S11}$$

with equilibrium fractions f_e and f_i. With either the full DEXSY or the rapid measurement, exchanging fractions as a function of mixing time can be fit with a 3-parameter model of the form

$$f(t_m) = (f_{SS} - f_0)\left[1 - e^{-k t_m}\right] + f_0 \tag{S12}$$

to estimate the initial exchange fraction $f_0 = 2 f_{i,e0}$, the steady-state exchange fraction $f_{SS} = \frac{2 f_i k_{i,e}}{k_{i,e} + k_{e,i}}$, and the characteristic exchange rate $k = k_{i,e} + k_{e,i}$ (called the apparent exchange rate, AXR, in the text).
The data we present calls for a nonzero initial condition. A previous study of T_2–T_2 exchange in a polymer–solvent system near the glass transition also observed finite exchange when $t_m \approx 0$ (32). Models have shown significant exchange during the encoding periods τ can lead to exchange peaks at $t_m = 0$ (33).

Bibliography

1. MD Hürlimann, KG Helmer, TM de Swiet, and PN Sen. Spin echoes in a constant gradient and in the presence of simple restriction. *Journal of Magnetic Resonance*, 113:260–264, 1995.
2. Denis S Grebenkov. NMR survey of reflected brownian motion. *Reviews of Modern Physics*, 79(3):1077, 2007.
3. Erwin L Hahn. Spin echoes. *Physical review*, 80(4):580, 1950.
4. Herman Y Carr and Edward M Purcell. Effects of diffusion on free precession in nuclear magnetic resonance experiments. *Physical review*, 94(3):630, 1954.
5. Donald E Woessner. Effects of diffusion in nuclear magnetic resonance spin-echo experiments. *The Journal of Chemical Physics*, 34(6):2057–2061, 1961.
6. John E Tanner. Transient diffusion in a system partitioned by permeable barriers. application to NMR measurements with a pulsed field gradient. *The Journal of Chemical Physics*, 69(4):1748–1754, 1978.
7. Denis le Bihan, Eric Breton, Denis Lallemand, Philippe Grenier, Emmanuel Cabanis, and Maurice Laval-Jeantet. MR imaging of intravoxel incoherent motions: application to diffusion and perfusion in neurologic disorders. *Radiology*, 161(2):401–407, 1986.
8. Nicolas Moutal, Kerstin Demberg, Denis S. Grebenkov, and Tristan Anselm Kuder. Localization regime in diffusion nmr: Theory and experiments. *Journal of Magnetic Resonance*, 305:162 – 174, 2019. ISSN 1090-7807. doi: https://doi.org/10.1016/j.jmr.2019.06.016.
9. S. D. Stoller, W. Happer, and F. J. Dyson. Transverse spin relaxation in inhomogeneous magnetic fields. *Phys. Rev. A*, 44:7459–7477, Dec 1991. doi: 10.1103/PhysRevA.44.7459.
10. Thomas M de Swiet and Pabitra N Sen. Decay of nuclear magnetization by bounded diffusion in a constant field gradient. *The Journal of chemical physics*, 100(8):5597–5604, 1994.
11. Richard Conable Wayne and Robert M Cotts. Nuclear-magnetic-resonance study of self-diffusion in a bounded medium. *Physical Review*, 151(1):264, 1966.
12. Baldwin Robertson. Spin-echo decay of spins diffusing in a bounded region. *Physical Review*, 151(1):273, 1966.
13. CH Neuman. Spin echo of spins diffusing in a bounded medium. *The Journal of Chemical Physics*, 60(11):4508–4511, 1974.
14. KJ Carlton, MR Halse, and John H Strange. Diffusion-weighted imaging of bacteria colonies in the strafi plane. *Journal of Magnetic Resonance*, 143(1):24–29, 2000.
15. Sarah L Codd and Paul T Callaghan. Spin echo analysis of restricted diffusion under generalized gradient waveforms: planar, cylindrical, and spherical pores with wall relaxivity. *Journal of Magnetic Resonance*, 137(2):358–372, 1999.
16. Brett N Ryland and Paul T Callaghan. Spin echo analysis of restricted diffusion under generalized gradient waveforms for spherical pores with relaxivity and interconnections. *Israel journal of chemistry*, 43(1-2):1–7, 2003.
17. Carin Malmborg, Daniel Topgaard, and Olle Söderman. NMR diffusometry and the short gradient pulse limit approximation. *Journal of Magnetic Resonance*, 169(1):85–91, 2004.
18. Alexandru V Avram, Evren Özarslan, Joelle E Sarlls, and Peter J Basser. In vivo detection of microscopic anisotropy using quadruple pulsed-field gradient (qpfg) diffusion MRI on a clinical scanner. *Neuroimage*, 64:229–239, 2013.
19. John Crank. *The mathematics of diffusion.* Oxford university press, 1979.
20. Teddy X Cai, Dan Benjamini, Michal E Komlosh, Peter J Basser, and Nathan H Williamson. Rapid detection of the presence of diffusion exchange. *Journal of Magnetic Resonance*, 297:17–22, 2018.
21. D.G. Rata, F. Casanova, J. Perlo, D.E. Demco, and B. Blümich. Self-diffusion measurements by a mobile single-sided NMR sensor with improved magnetic field gradient. *Journal of Magnetic Resonance*, 180(2):229 – 235, 2006. ISSN 1090-7807. doi: https://doi.org/10.1016/j.jmr.2006.02.015.
22. Saul Meiboom and David Gill. Modified spin-echo method for measuring nuclear relaxation times. *Review of scientific instruments*, 29(8):688–691, 1958.
23. Federico Casanova, Juan Perlo, and Bernhard Blümich. *Single-sided NMR.* Springer, 2011.
24. K. E. Washburn and P. T. Callaghan. Tracking pore to pore exchange using relaxation exchange spectroscopy. *Physical Review Letters*, 97:175502, Oct 2006.
25. P. T. Callaghan and I. Furó. Diffusion-diffusion correlation and exchange as a signature for local order and dynamics. *The Journal of Chemical Physics*, 120(8):4032–4038, 2004.
26. Ruobing Song, Yi-Qiao Song, Muthusamy Vembusubramanian, and Jeffrey L. Paulsen. The robust identification of exchange from T2—T2 time-domain features. *Journal of Magnetic Resonance*, 265:164 – 171, 2016. ISSN 1090-7807.
27. Martin D Hürlimann. Diffusion and relaxation effects in general stray field NMR experiments. *Journal of Magnetic Resonance*, 148(2):367–378, 2001.

bioRxiv preprint doi: https://doi.org/10.1101/694661; this version posted November 21, 2019. The copyright holder for this preprint (which was not certified by peer review) is the author/funder. All rights reserved. No reuse allowed without permission.

28. Ruiliang Bai, Andreas Klaus, Tim Bellay, Craig Stewart, Sinisa Pajevic, Uri Nevo, Hellmut Merkle, Dietmar Plenz, and Peter J Basser. Simultaneous calcium fluorescence imaging andMR of ex vivo organotypic cortical cultures: a new test bed for functionalMRI. *NMR in Biomedicine*, 28(12):1726–1738, 2015.
29. Jan Watzlaw, Stefan Glöggler, Bernhard Blümich, Wilfried Mokwa, and Uwe Schnakenberg. Stacked planar micro coils for single-sided NMR applications. *Journal of Magnetic Resonance*, 230: 176–185, 2013.
30. Alexandre A Khrapitchev and Paul T Callaghan. Double NMR with stimulated echoes: phase cycles for the selection of desired encoding. *Journal of Magnetic Resonance*, 152(2):259–268, 2001.
31. Oliver Neudert, Siegfried Stapf, and Carlos Mattea. Diffusion exchange NMR spectroscopy in inhomogeneous magnetic fields. *Journal of Magnetic Resonance*, 208(2):256–261, 2011.
32. Nathan H Williamson, April M Dower, Sarah L Codd, Amber L Broadbent, Dieter Gross, and Joseph D Seymour. Glass dynamics and domain size in a solvent-polymer weak gel measured by multidimensional magnetic resonance relaxometry and diffusometry. *Physical review letters*, 122(6):068001, 2019.
33. L. M. Schwartz, D. L. Johnson, J. Mitchell, T. C. Chandrasekera, and E. J. Fordham. Modeling two-dimensional magnetic resonance measurements in coupled pore systems. *Phys. Rev. E*, 88: 032813, Sep 2013. doi: 10.1103/PhysRevE.88.032813.
34. H Hasko Paradies. Shape and size of a nonionic surfactant micelle. triton x-100 in aqueous solution. *The Journal of Physical Chemistry*, 84(6):599–607, 1980.

bioRxiv preprint doi: https://doi.org/10.1101/694661; this version posted November 21, 2019. The copyright holder for this preprint (which was not certified by peer review) is the author/funder. All rights reserved. No reuse allowed without permission.

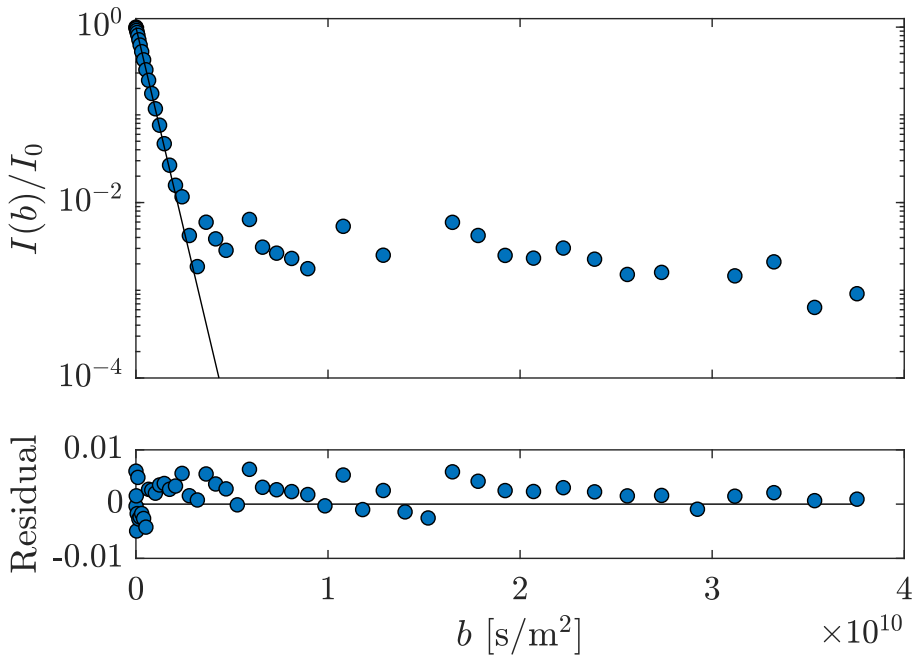

Fig. S1. 1-D diffusion data, single exponential fit and residuals for aCSF at 25°C, 50 points. A fit of the first 15 points, attenuating the signal to $I/I_0 = 0.1$, provides $D_0 = 2.153 \pm 0.014 \times 10^{-9}\ \mathrm{m}^2/\mathrm{s}$ from three measurements.

bioRxiv preprint doi: https://doi.org/10.1101/694661; this version posted November 21, 2019. The copyright holder for this preprint (which was not certified by peer review) is the author/funder. All rights reserved. No reuse allowed without permission.

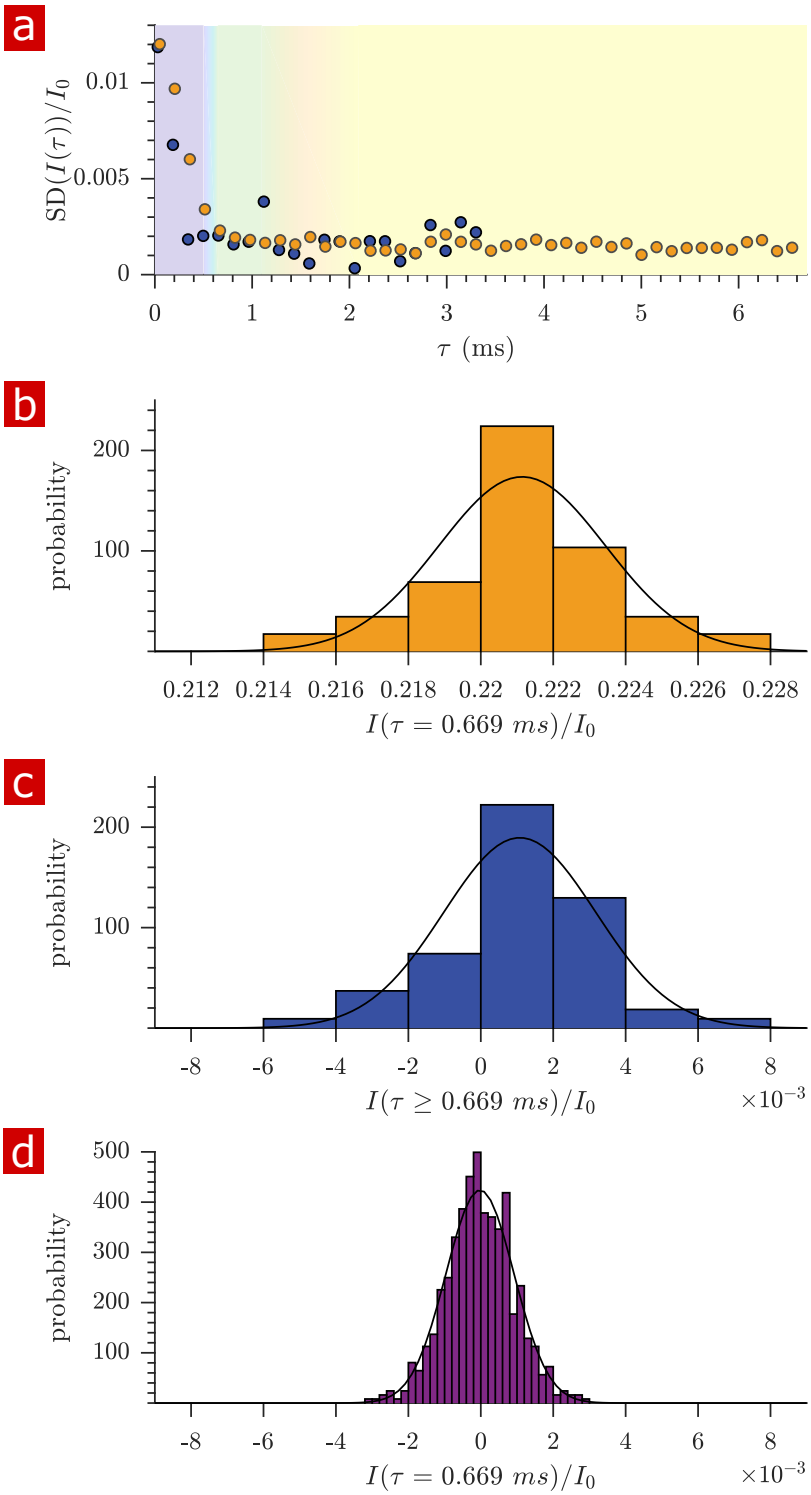

Fig. S2. Variability of diffusion data from measurements repeated on the same samples. a) Standard deviation (SD) of the signal intensity from 29 diffusion measurements, spaced 54 minutes apart, performed on a fixed spinal cord (orange) and three measurements performed back-to-back on aCSF (purple) at 25°C. Data is from the same samples as in Fig. 2 in the main manuscript. b) Histogram of signal intensity from measurements on the fixed spinal cord at $\tau = 0.669$ with mean±SD 0.2211 ± 0.0023. c) Histogram from the measurements on aCSF at $\tau \geq 0.669$, after signal has decayed away, with mean±SD 0.0011 ± 0.0021. d) Histogram of noise from 621 diffusion measurements performed on a dry chamber with nothing filling the solenoid coil, with mean±SD $-2 \times 10^{-5} \pm 0.001$. In (b), (c) and (d), Gaussian distributions are plotted using the mean and SD as parameters μ and σ. Note the similar window width in (b), (c), and (d) allow comparison of SD. Additional text on noise and SNR is provided in Supplementary Methods.

bioRxiv preprint doi: https://doi.org/10.1101/694661; this version posted November 21, 2019. The copyright holder for this preprint (which was not certified by peer review) is the author/funder. All rights reserved. No reuse allowed without permission.

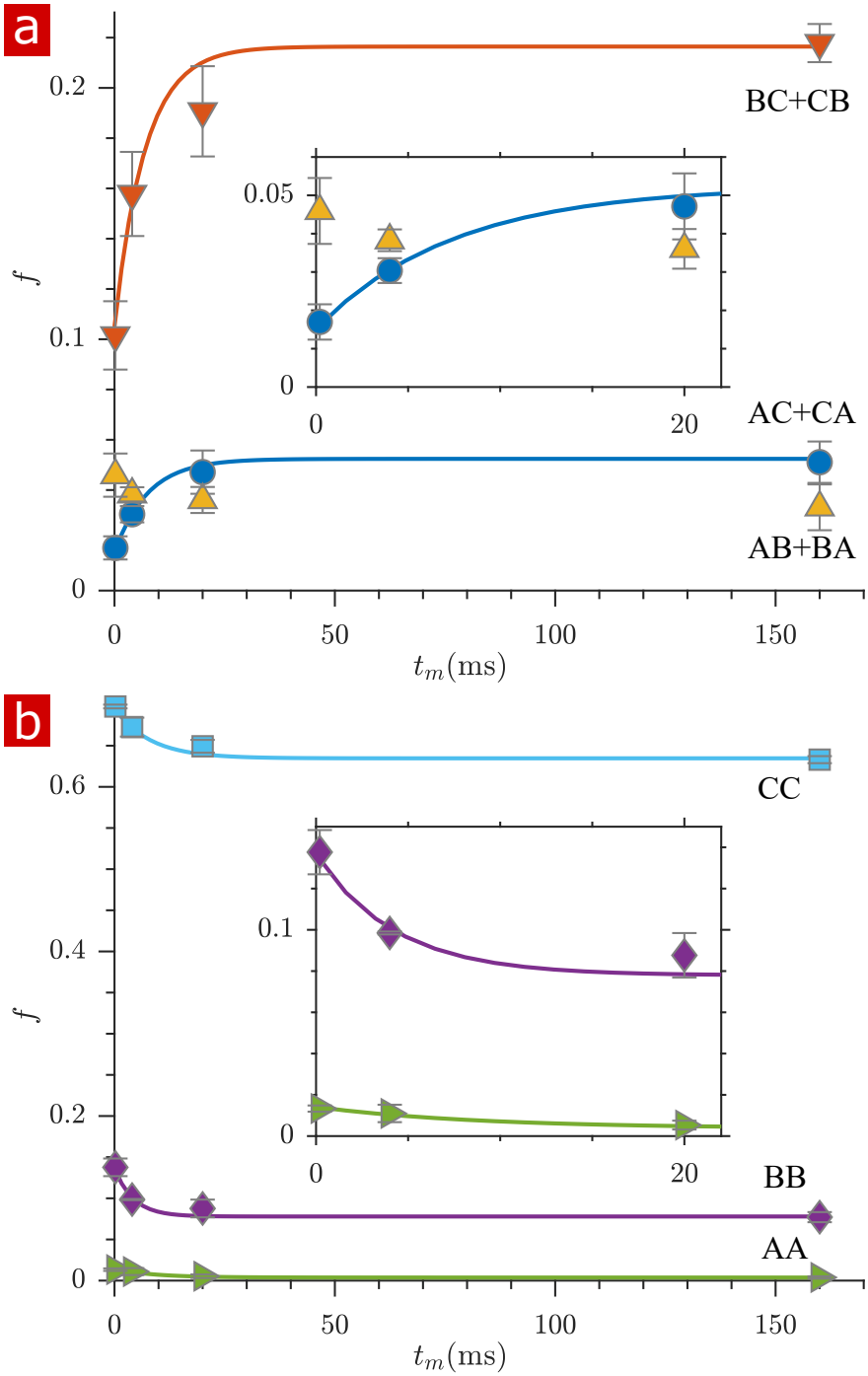

Fig. S3. Fractions of exchanging and non-exchanging water. a) Fractions of water which exchange between regions A, B, and C, (defined in Fig. 3) as a function of mixing time, t_m. Exchange fractions $f_{\mathrm{AC+CA}}$ and $f_{\mathrm{BC+CB}}$ are fit with a first order rate model with estimated apparent exchange rates AXRs (mean±standard deviation from three measurements) 140 ± 80 and 140 ± 140 s^{-1} respectively. $f_{\mathrm{AB+BA}}$ does not follow the expected first order rate model. b) Fractions of non-exchanging water. Non-exchange fractions f_{AA}, f_{BB}, and f_{CC} are fit with a first order rate model with estimated AXRs 110 ± 100 , 230 ± 170 , and 130 ± 100 s^{-1} respectively. Insets zoom in on the initial rise in exchange. Error bars are the standard deviations from three repeat measurements.

bioRxiv preprint doi: https://doi.org/10.1101/694661; this version posted November 21, 2019. The copyright holder for this preprint (which was not certified by peer review) is the author/funder. All rights reserved. No reuse allowed without permission.

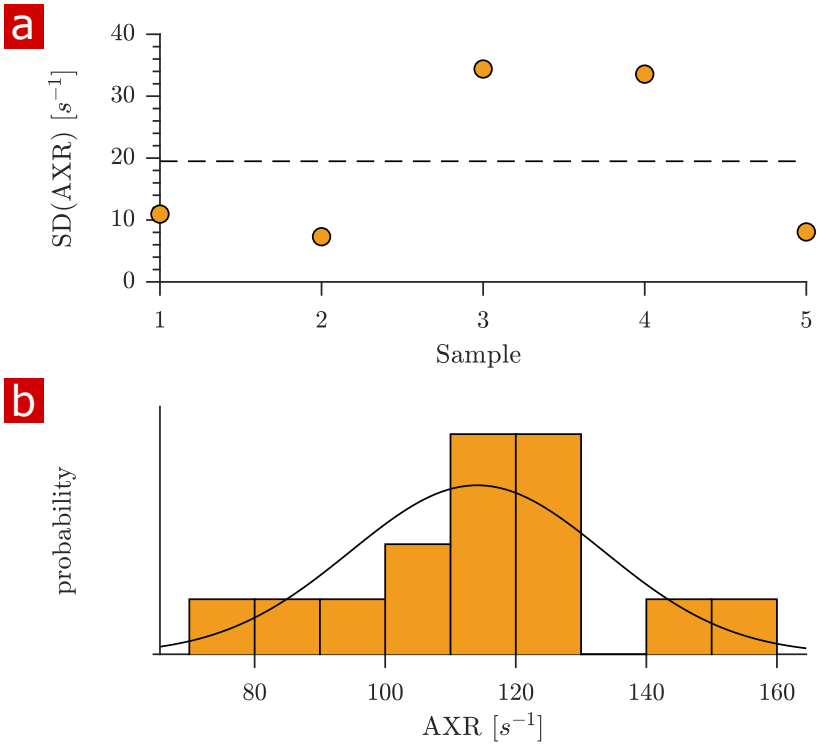

Fig. S4. Variability of apparent exchange rates (AXRs). a) Standard deviations of AXRs from three rapid exchange measurements shown for five fixed spinal cord samples. The dashed line shows the SD from all (3×5) measurements. b) Histogram of all measured AXRs with mean=114 and SD=19 s^{-1}. A Gaussian distributions are plotted using the mean and SD as parameters μ and σ. An Anderson–Darling test indicate that the distribution is not dissimilar from a Gaussian distribution ($P = 0.88 > 0.05$).

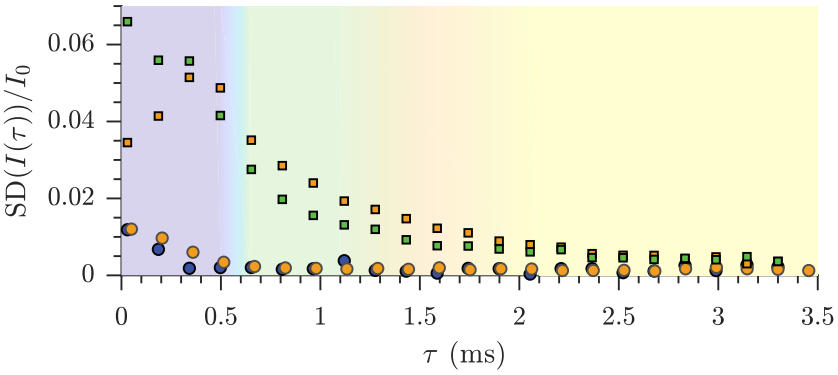

Fig. S5. Sample-to-sample variability of diffusion data. Standard deviations of the diffusion signal attenuation are presented for live (n=9) (green squares) and fixed (n=6) (orange circles) sample groups. The standard deviations from repeated measurements are also re-plotted from Fig. S2. The sample-to-sample variability is higher that the variability of repeated measurements due to structural and size differences between samples and the sensitivity of the measurement to these differences.

bioRxiv preprint doi: https://doi.org/10.1101/694661; this version posted November 21, 2019. The copyright holder for this preprint (which was not certified by peer review) is the author/funder. All rights reserved. No reuse allowed without permission.

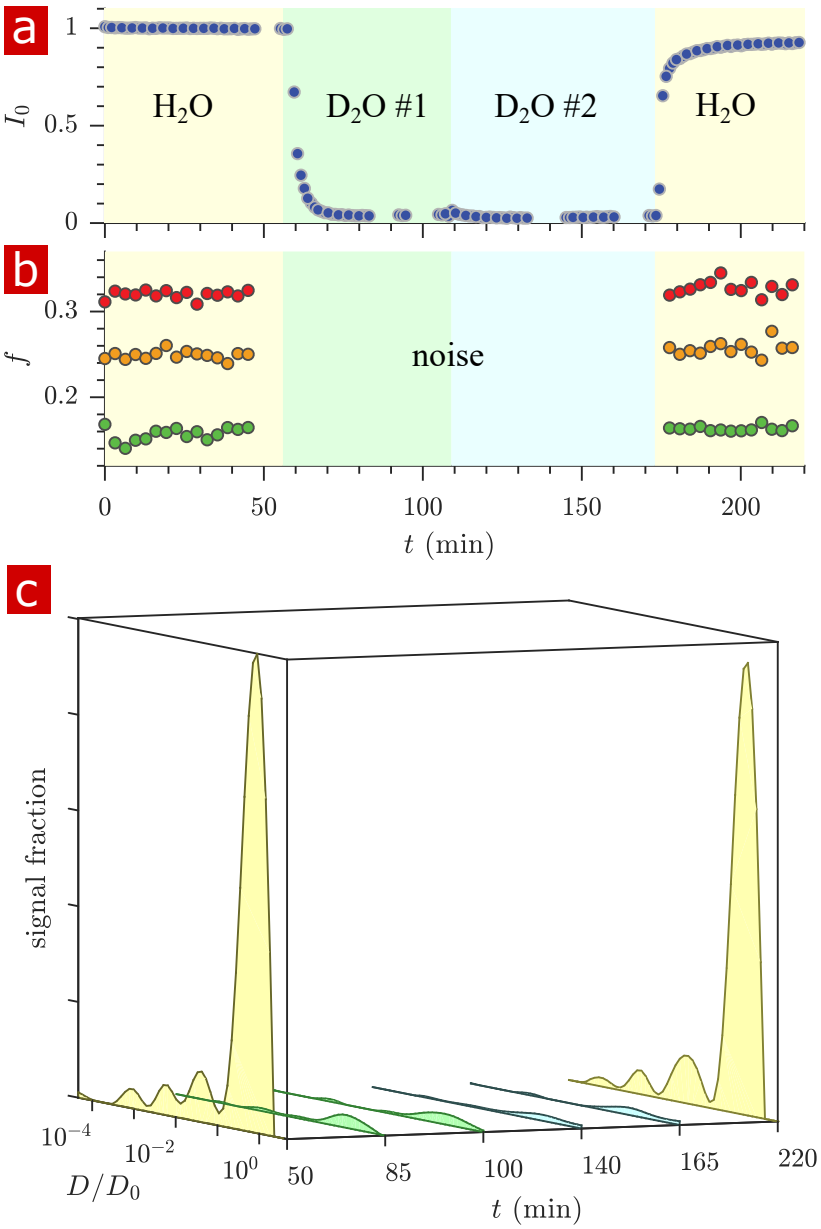

Fig. S6. Timecourse study of D_2O wash. The sample was washed from aCSF to aCSF made with deuterated water in two steps and back to aCSF as shown by the pastel color yellow, green, blue, and yellow shadings for H_2O, D_2O #1, D_2O #2, and H_2O. a) The proton signal intensity from the rapid exchange measurement data normalized to remove T_1 effects at different mixing times. b) Exchanging fractions from rapid measurements with $t_m = 0.2$ (blue), 4 (red), and 20 ms (orange). 1-D diffusion measurements were performed at points throughout the time-course (seen as breaks in the data in (a) and (b)) and distributions are presented as signal fractions ($P(D) \times I_0$) in (c). All distribution peaks decreased after washing with D_2O indicating that the distribution is indicative of water mobility, with no single component being solely from non-water molecules.

bioRxiv preprint doi: https://doi.org/10.1101/694661; this version posted November 21, 2019. The copyright holder for this preprint (which was not certified by peer review) is the author/funder. All rights reserved. No reuse allowed without permission.

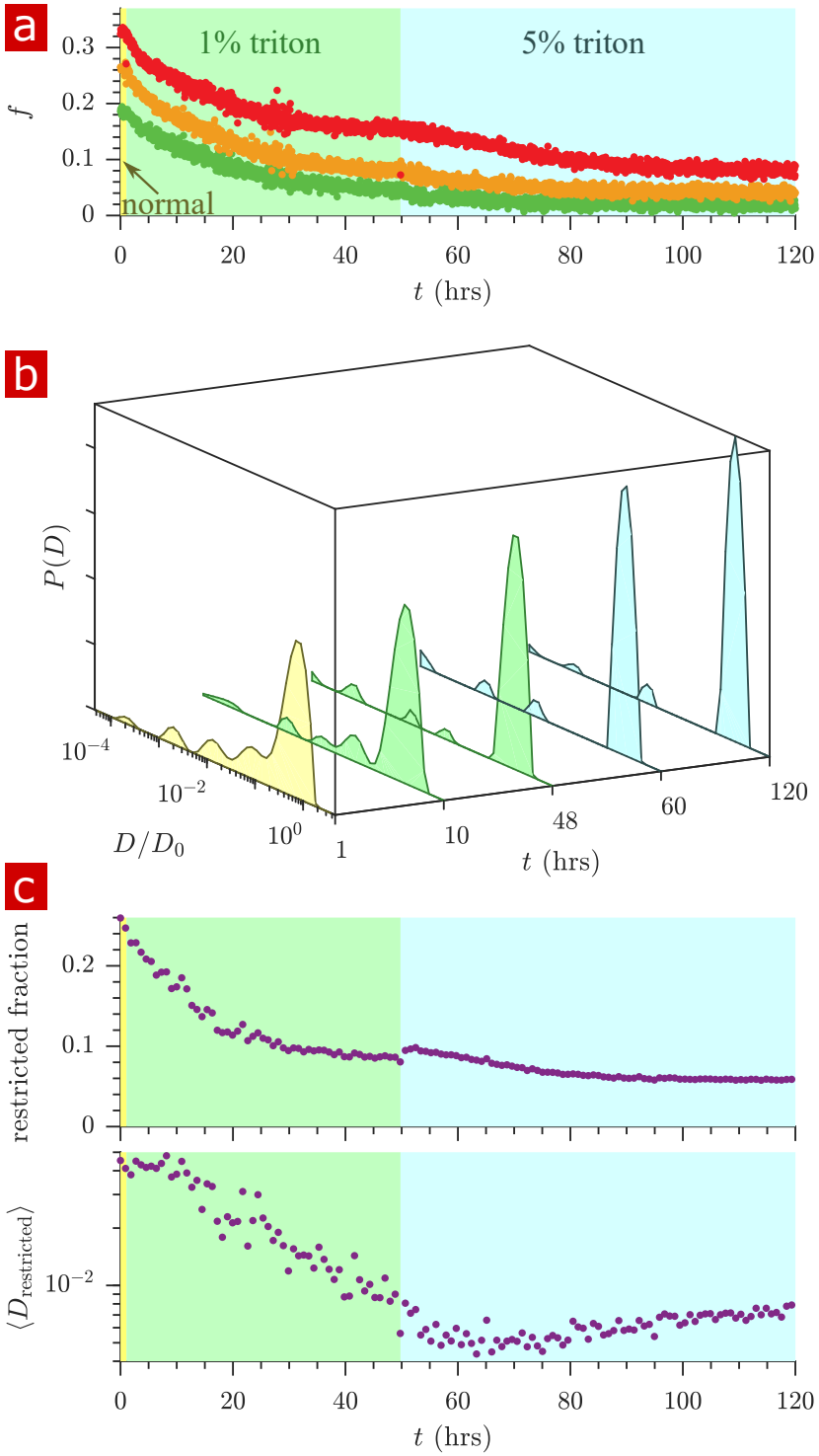

Fig. S7. Timecourse study of Triton X delipidation The sample was washed to aCSF with 1% Triton X, and then 5% Triton X showing a) exchanging fractions from rapid measurements with $t_m = 0.2$ (green), 4 (orange), and 20 ms (red), b) representative distributions throughout the timecourse, and c) the fraction and mean diffusion coefficient of signal arising from restricted water ($\langle D_{\text{restricted}} \rangle$ with $D/D_0 < 0.17$). A bump in the restricted fraction seen upon addition of the 5% Triton is due to the Triton X itself which forms 5 nm micelles (34). The loss of the restricted diffusion peaks and the decrease in the exchanging fractions shows that membranes are the cause of water restriction.

bioRxiv preprint doi: https://doi.org/10.1101/694661; this version posted November 21, 2019. The copyright holder for this preprint (which was not certified by peer review) is the author/funder. All rights reserved. No reuse allowed without permission.

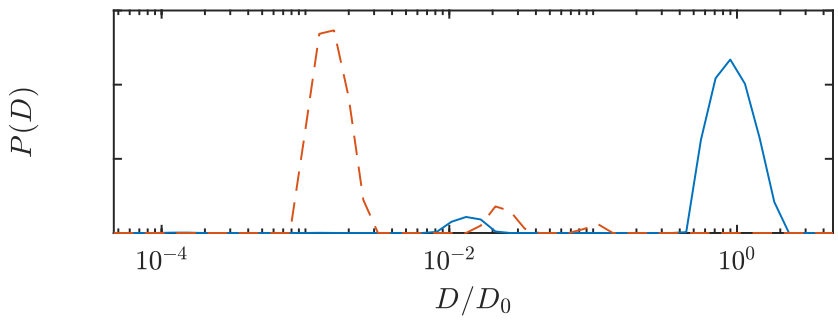

Fig. S8. Diffusion coefficient distributions of 5% Triton X in aCSF (solid blue line) and pure Triton (dashed red line). The standard diffusion measurement protocol (43 pts. $\tau = 0.05 \rightarrow 6.6$ ms) was used. The 5% Triton X shows an additional peak at $D/D_0 = 0.013$ due to formation of 5 nm micelles (34). Pure Triton X shows a major diffusion coefficient component at $D/D_0 = 0.001$.

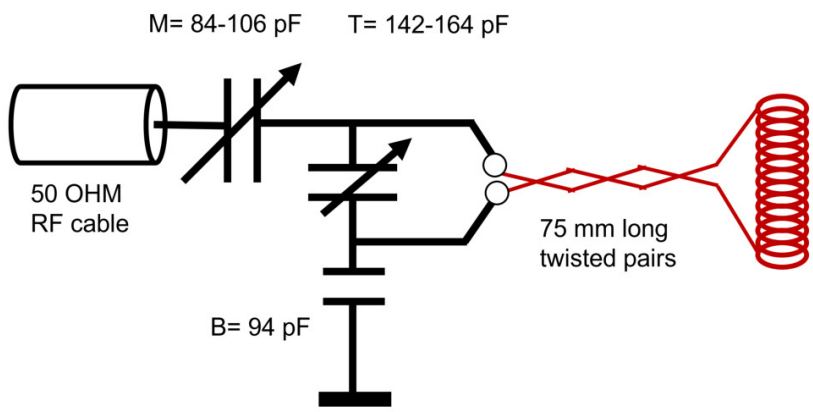

Fig. S9. RF circuit design. Drawing of the circuit for the RF showing the capacitance of the tune (T), match (M), and balance (B). Note a single wrapping of the solenoid was drawn rather than the actual double-wrap for visual simplicity.

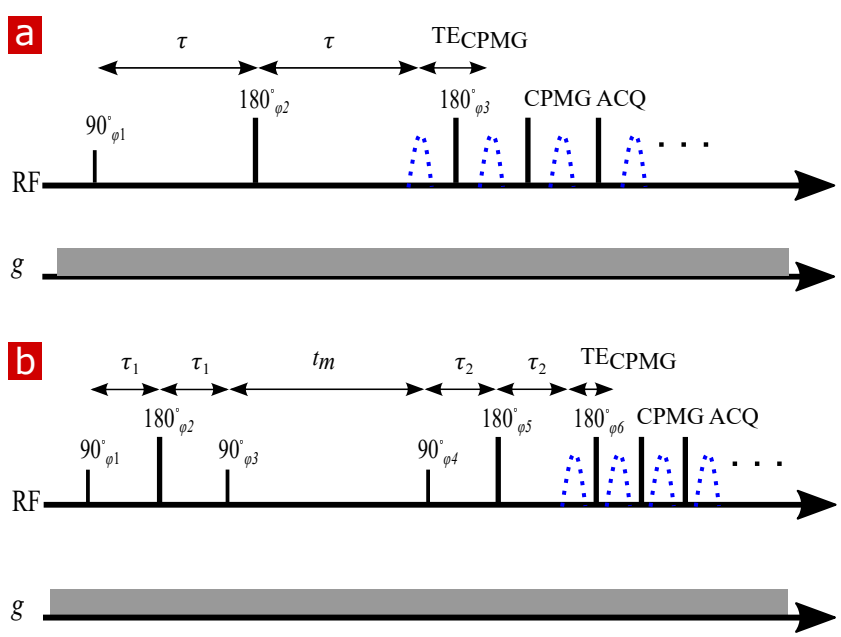

Fig. S10. NMR diffusion and exchange pulse sequences. a) Spin echo pulse sequence for measuring diffusion with a static gradient. τ is varied to control b. (b) DEXSY pulse sequence for measuring exchange with a static gradient. The two SE encoding blocks with τ_1 and τ_2, varied independently to control b_1 and b_2, are separated by t_m. Signal is acquired in a CPMG train for both (a) and (b).

bioRxiv preprint doi: https://doi.org/10.1101/694661; this version posted November 21, 2019. The copyright holder for this preprint (which was not certified by peer review) is the author/funder. All rights reserved. No reuse allowed without permission.

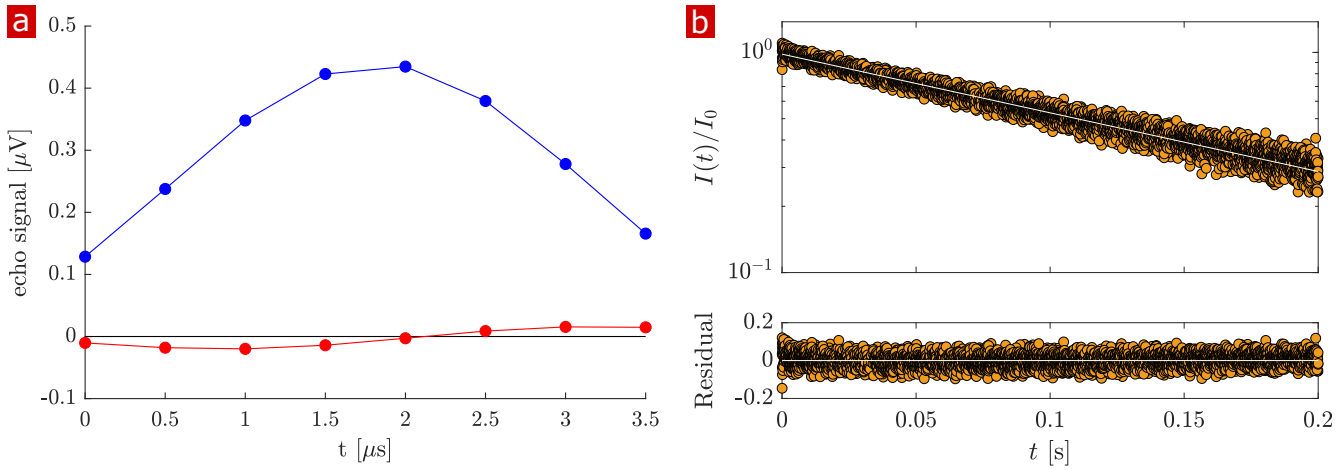

Fig. S11. T_2 **measurement.** Representative Carr-Purcell-Meiboom-Gill (CPMG) (10 s repetition time (TR), 8000 echoes) on fixed spinal cord. a) The echo shape summed over all echoes (real signal (blue) phased maximum and imaginary signal phased to zero (red)). b) Real signal decay (orange circles) and exponential fit with $T_2 = 163$ ms and $I_0 = 6.5\mu\mathrm{V}$ (white line) and residuals of the fit.

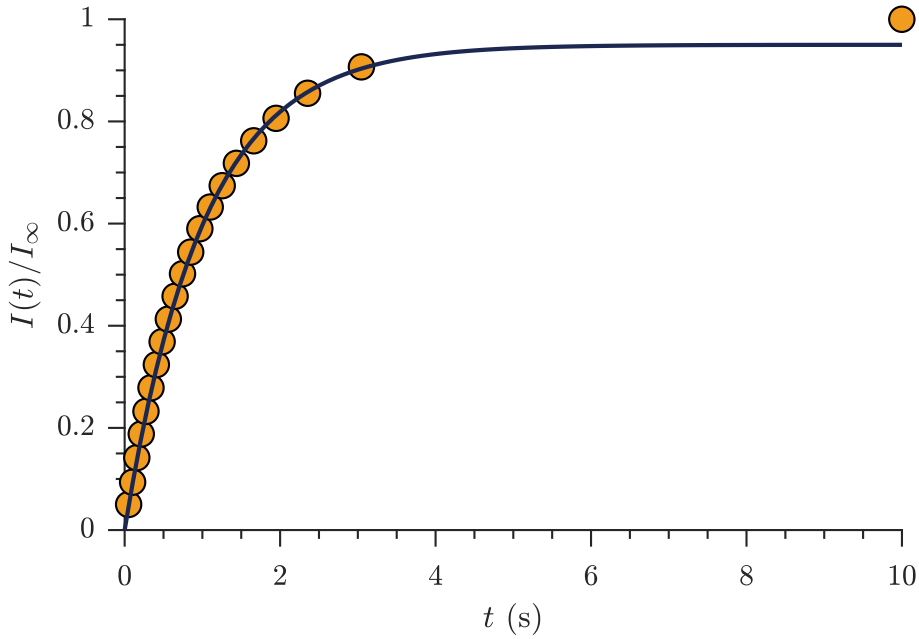

Fig. S12. T_1 **measurement.** Representative saturation recovery experiment on fixed spinal cord (1s TR, 21 recovery time pts. logarithmically spaced from 50 ms to 10 s) showing signal intensity normalized by signal at 10 s recovery time (orange circles) and exponential fit with estimated $T_1 = 990$ ms (solid black line).

bioRxiv preprint doi: https://doi.org/10.1101/694661; this version posted November 21, 2019. The copyright holder for this preprint (which was not certified by peer review) is the author/funder. All rights reserved. No reuse allowed without permission.

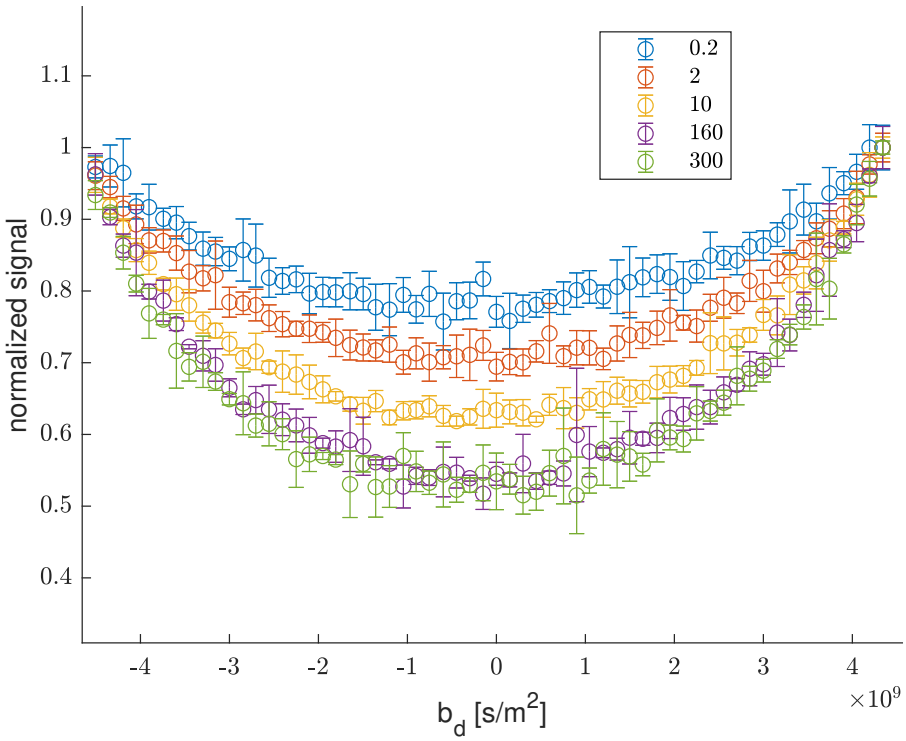

Fig. S13. Rapid exchange tests #1. The curvature along slices of $b_s = 4500\ \mathrm{s/mm^2}$ as a function of b_d highlighting the increase in the depth of the curvature with increasing t_m, shown in figure legend. The increased depth is due to increased exchange (20, 26)

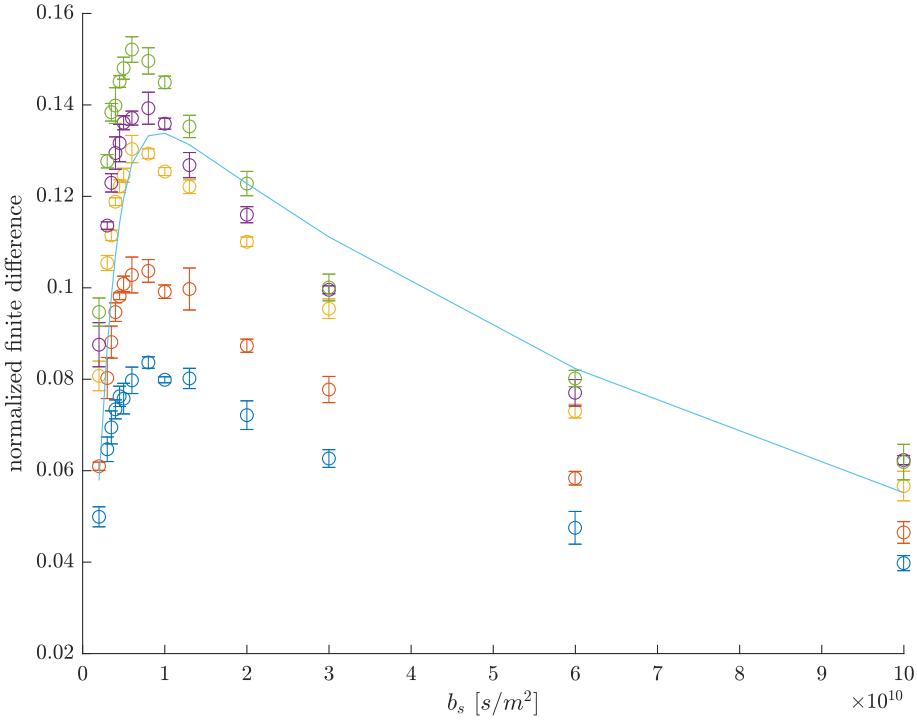

Fig. S14. Rapid exchange tests #2. Difference between $2I_{b_d=0}$ and $I_{bd=+bs} + I_{bd=-bs}$, normalized by $I_{0,0}$, a function of b_s, showing the optimal b_s for measuring the largest curvature response as occurring near $b_s = 6000\ \mathrm{s/mm^2}$. The line is a prediction of the finite difference for a two-site system, from Eq. 8 in Ref. (20) using $f = 0.15$, $D_e = 10^{-9}$, and $D_i = 10^{-11}\ \mathrm{s/mm^2}$.

bioRxiv preprint doi: https://doi.org/10.1101/694661; this version posted November 21, 2019. The copyright holder for this preprint (which was not certified by peer review) is the author/funder. All rights reserved. No reuse allowed without permission.

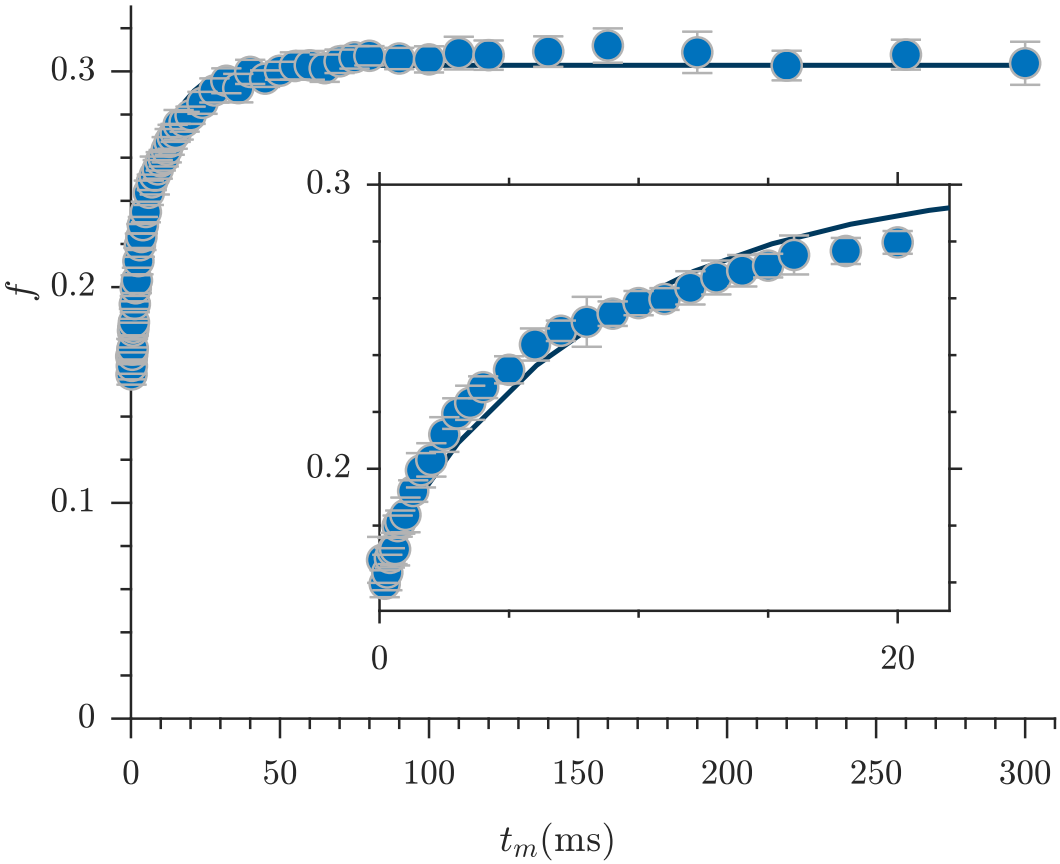

Fig. S15. Rapid exchange tests #3. High temporal resolution exchange rate measurement from the rapid measurement with $b_s = 4500\,\mathrm{s/mm}^2$ and 53 t_m points between 0.1 and 300 ms. First order rate model fits estimate AXR=$113.7 \pm 5.2\ s^{-1}$ (solid line).